UNIVERSIDAD DE CONCEPCIÓN
FACULTAD DE CIENCIAS FÍSICAS Y MATEMÁTICAS

A LONG TERM PHOTOMETRIC ANALYSIS OF THE CLOSE INTERACTING BINARY SX CAS

New insights into the system evolution

Por: Vicente E. Acuña Machuca

Tesis presentada a la Facultad de Ciencias Físicas y Matemáticas de la Universidad de Concepción para optar al grado académico de Magíster en Astronomía

Julio 2026
Concepción, Chile

Profesor Guía: Dr. Ronald Mennickent Cid

Dedicado a mi familia, amigos y entorno deportivo.

AGRADECIMIENTOS

Este proyecto fue financiado por ANID-Subdirección de capital humano/Magíster Nacional/2022-22221588

Primero que todo quiero agradecer a mi entorno familiar, el cual me ha apoyado incondicionalmente durante todo este proceso. Gracias por soportar mis actitudes y mi especial forma de ser.

A continuación agradecer al equipo de directiva y entrenadores de la rama de tenis de mesa del club deportivo Huachipato por permitirme ser parte del increíble grupo humano que se gesta ahí. El tenis de mesa ha sido y será un pilar muy importante dentro de mi vida.

Agradecer la disposición de mis amigos, en especial a los del grupo "Los impulsivos" y a Melanie Riquelme, personas que me han brindado un apoyo más que necesitado durante épocas difíciles, y que sin duda no estaría aquí sin ellos.

Finalmente, agradecer a mi equipo de apoyo psicológico, psicólogo Matías Ortiz y doctor Jonathan Campillo, personas que me ayudaron a salir adelante cuando las situaciones se pusieron difíciles.

Muchas gracias a todos.

Resumen

El estudio de los sistemas estelares binarios es crucial para avanzar en nuestra comprensión de la astrofísica estelar. Una subclase notable corresponde a las Variables de Doble Período (DPV, por sus siglas en inglés), sistemas binarios interactuantes que presentan un segundo ciclo fotométrico característico, típicamente del orden de ~ 33 veces su período orbital. Los mecanismos físicos responsables de este segundo ciclo permanecen aún como un problema abierto.

En este trabajo estudiamos la curva de luz fotométrica del complejo sistema binario interactuante SX Cas. A pesar de su interés astrofísico, este sistema no ha sido objeto de un estudio exhaustivo en casi dos décadas. El objetivo de este trabajo es contribuir a cerrar esta brecha mediante la derivación y actualización de los parámetros orbitales y físicos del sistema, combinando bases de datos fotométricas modernas previamente inexploradas con observaciones de archivo disponibles en la literatura. En particular, construimos por primera vez una curva de luz de largo plazo, cubriendo aproximadamente 117 años de observaciones.

Realizamos tres análisis principales: un estudio de variaciones de período mediante diagramas O–C, un análisis de periodicidad utilizando múltiples técnicas de periodogramas (PDM, GLS y WWZ), y un modelado de curvas de luz orientado a determinar los parámetros físicos fundamentales del sistema. Nuestros resultados sugieren que el sistema presenta variaciones complejas en su período orbital. Además, los datos más recientes revelan la posible presencia de un segundo ciclo fotométrico de mayor escala temporal, consistente con el comportamiento observado en sistemas tipo DPV, aunque su naturaleza y estabilidad requieren confirmación adicional. Asimismo, encontramos indicios de una posible correlación entre este ciclo largo y cambios morfológicos en la estructura del disco de acreción, la cual debe ser interpretada con cautela.

SX Cas emerge como un sistema notablemente complejo, y los resultados presentados en este trabajo aportan nuevas restricciones observacionales para comprender su naturaleza y la evolución a largo plazo de discos de acreción en sistemas binarios interactuantes.

Palabras clave – Astrofísica estelar, evolución de sistemas binarios, sistemas binarios interactuantes, discos de acreción.

Abstract

The study of binary star systems is fundamental for advancing our understanding of stellar astrophysics. A notable subclass is that of Double Periodic Variables (DPVs), interacting binaries that exhibit a long photometric cycle typically of the order of ~ 33 times their orbital period. The physical mechanisms responsible for this secondary cycle remain an open problem.

In this work, we analyze the photometric light curve of the complex interacting binary system SX Cas. Despite its astrophysical relevance, the system has not been the subject of a dedicated and comprehensive study in nearly two decades. The aim of this work is to help bridge this gap by deriving updated orbital and physical parameters of SX Cas, combining previously unexplored modern photometric surveys with archival observations from the literature. In particular, we construct, for the first time, a long-term photometric light curve spanning approximately 117 years of data.

We perform three main analyses: a period-change study using O–C diagrams, a periodicity analysis employing multiple periodogram techniques (PDM, GLS, and WWZ), and a light-curve modeling approach aimed at constraining the fundamental physical parameters of the system. Our results suggest that the system exhibits complex orbital period variations. Furthermore, the most recent data reveal the possible presence of a longer photometric cycle, consistent with DPV-like behavior, although its nature and stability remain to be confirmed. We also find tentative evidence for structural changes in the accretion disk during the long cycle, which should be interpreted with caution.

SX Cas appears as a remarkably complex system, and the results presented here provide new observational constraints on its nature and on the long-term evolution of accretion disks in interacting binary systems.

Keywords – Stellar astrophysics, binary star evolution, close binary systems, accretion disks

Contents

List of Tables

List of Figures

Chapter 1

Introduction

1.1 Importance of the Study of Binary Systems

Most stars belong to gravitationally bound multiple systems (Duchêne & Kraus 2013). Among them, binary systems — pairs of stars bound by mutual gravity — offer some of the most direct means of measuring fundamental stellar parameters, such as mass, radius, effective temperature, and luminosity, through combined photometric and spectroscopic techniques (Andersen 1991; Torres et al. 2010).

Binary interaction plays a pivotal role in stellar evolution: for example, more than 70% of massive stars undergo mass exchange with a companion, and roughly one-third of these interactions ultimately result in stellar mergers (Sana et al. 2012). Furthermore, approximately 30% of massive main-sequence stars are thought to be products of binary interactions (de Mink et al. 2014). Understanding these processes is essential not only for tracing the evolutionary pathways of massive stars, but also for explaining phenomena such as the multiple stellar populations observed in certain globular clusters (Jiang et al. 2014; Wei et al. 2020, 2021). Moreover, binary interactions govern how systems evolve toward their late stages, and in the case of massive stars can lead to some of the most energetic events in the Universe, including supernovae and gamma-ray bursts.

1.2 Theoretical Context

1.2.1 The Physics of Binary Systems

The standard physical framework for interacting binary stars is the Roche model (Roche 1849, 1851; Kopal 1959). In this model, each star is approximated as a point mass, and an effective potential — comprising the gravitational and centrifugal components arising from the orbital motion — defines a set of equipotential surfaces. A particular equipotential surface encloses the so-called Roche lobe of each component, within which material is gravitationally bound to that star (see Fig. 1.2.1). The relative shape of each lobe depends only on the mass ratio $q = M_2/M_1$. Following Eggleton (1983), the volume-equivalent radius of a Roche lobe for the primary star (M_1) in units of the orbital separation can be approximated by

$$R_L = \frac{0.49\, q^{-2/3}}{0.6\, q^{-2/3} + \ln(1 + q^{-1/3})}. \tag{1.2.1}$$

Binary systems are commonly classified according to the degree of Roche-lobe filling: detached (neither star fills its lobe), semi-detached (one star fills its lobe), contact (both stars fill their lobes but retain separate envelopes), and common-envelope (both stars fill their lobes and share a common envelope). The right panel of Fig. 1.2.1 illustrates these configurations. In a semi-detached system, the star filling its Roche lobe may transfer material through the inner Lagrangian point L_1. Depending on the mass ratio and the stellar radii, the transferred stream either impacts the gainer directly or circulates to form an accretion disk (Lubow & Shu 1975). Such disks in eclipsing binaries can leave distinctive imprints on the photometric light curve, enabling detailed determination of system parameters (e.g., Djurasevic 1992; Mennickent 2017).

During mass transfer, the orbital period may change depending on whether the process is conservative (mass and angular momentum are conserved) or non-conservative (mass and/or angular momentum are lost from the system) (de Miguel et al. 2018). Consequently, long-term monitoring of eclipse timings via the Observed-Calculated (O–C) technique provides valuable constraints on the mass transfer and angular momentum evolution in interacting binaries.

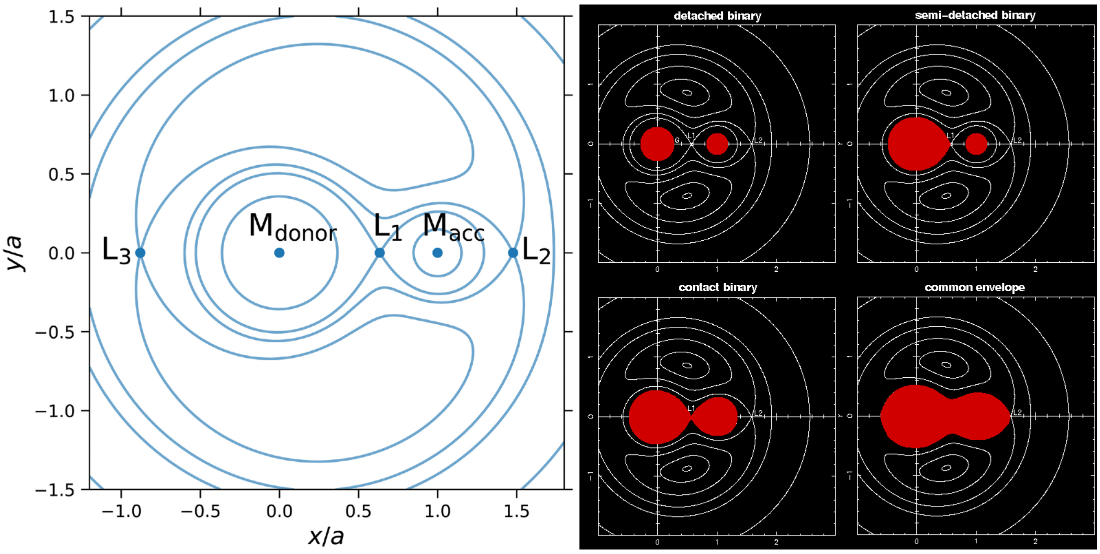

Figure 1.2.1: *Left panel:* Equipotential lines of the Roche potential for a binary with mass ratio $q = 0.26$ and orbital separation a (Misra et al. 2020). *Right panel:* Classification of binaries according to Roche-lobe filling states.

1.2.2 Eclipsing Binaries

Binary systems may also be detected and classified on the basis of their observational signatures. These include visual binaries (both components are spatially resolved), spectroscopic binaries (identified by periodic Doppler shifts in their spectra), eclipsing binaries (in which the orbital inclination produces mutual eclipses and corresponding photometric variability), and astrometric binaries (in which one component appears to orbit an unseen companion, such as a compact object). The orbital and stellar parameters of these systems can be inferred by applying Newton's and Kepler's laws.

Eclipsing binaries are observationally classified into three subtypes: EA (Algol-type), characterized by relatively flat light-curve segments between eclipses; EB (β Lyrae-type), with continuously varying and smoothly rounded light-curve shapes; and EW (W UMa-type), in which the primary and secondary eclipse depths are nearly indistinguishable. Although this classification is purely observational, it often correlates — albeit not uniquely — with the underlying physical configuration of the system (see Fig. 1.2.2). Importantly, eclipsing systems allow direct measurement of individual stellar masses and radii when combined with radial-velocity data, making them critical benchmarks for the calibration of stellar evolution models.

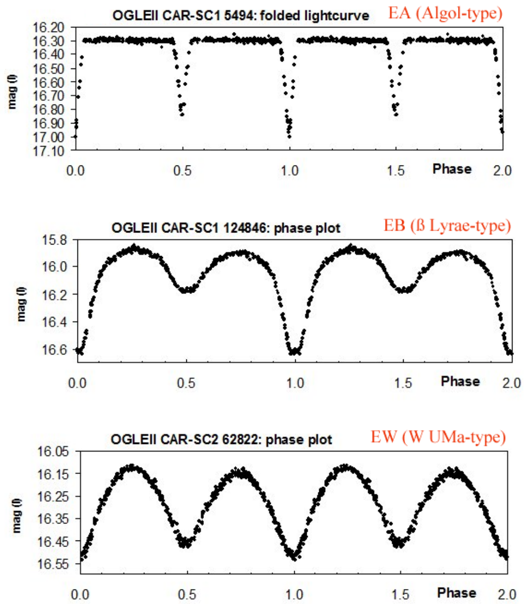

Figure 1.2.2: Light curves of different types of eclipsing binaries. *Top:* EA or Algol-type; *Middle:* EB or β Lyrae-type; *Bottom:* EW or W UMa-type (adapted from Hümmerich et al. 2013).

1.3 Double Periodic Variables

Double Periodic Variables (DPVs) are a subclass of interacting binary systems that exhibit two distinct photometric cycles: the short orbital period (P_{orb}) and a much longer superorbital cycle (P_{long}), typically 30 to 40 times the orbital period (Mennickent et al. 2003; Mennickent 2022). Recent work by Rosales et al. (2024) on V4142 Sgr modeled the system using the stellar evolution code MESA, finding evidence for a magnetic dynamo in the donor star; however, the resulting surface magnetic fields are too weak to account for the observed changes in the mass-transfer rate, so the dynamo should be regarded as a supporting, rather than dominant, ingredient in the DPV scenario. Additional large-sample analyses by Garcés et al. (2025) confirm that many DPVs display long-cycle period changes accompanied by corresponding variations in the morphology of their orbital light curves. Taken together, these findings establish DPVs as a key laboratory for investigating the interplay between mass transfer, accretion disk dynamics, and long-term cyclic behavior in interacting binary systems.

1.4 Motivation and This Work

An essential tool in studying interacting binaries is the eclipse timing analysis via the O–C (Observed minus Calculated) diagram, which tracks deviations of eclipse timings from a given ephemeris and thereby reveals period changes attributable to mass transfer, angular-momentum loss, third-body effects, or magnetic activity cycles. Although the O–C method is well established (e.g., Sterken 2005), recent high-precision space-based photometry and ground-based time-series surveys have substantially improved its sensitivity to subtle period modulations in interacting systems (Koch et al. 2022). Nevertheless, it is important to note that the interpretation of O–C variations is often degenerate, as multiple physical mechanisms can produce similar signatures.

The eclipsing system SX Cas (BD+54 7; 2MASS J00104207+5453293; $\alpha_{2000} = 00^{\mathrm{h}}10^{\mathrm{m}}42.068^{\mathrm{s}}$, $\delta_{2000} = +54°53'29.36''$; $V = 8.97$ mag; spectral types B5 + K3 III)[1] has an orbital period $P_{\mathrm{orb}} \approx 36.58$ d (Blažko 1908). The system comprises a mid-B primary ($5.1 \pm 0.4\,M_\odot$; $R = 3.0 \pm 0.4\,R_\odot$) and a cooler K3 III companion ($1.5 \pm 0.4\,M_\odot$; $R = 23.5 \pm 1.3\,R_\odot$) (Andersen et al. 1988). The hotter component is obscured by a geometrically and optically thick accretion disk, most likely fed by mass transfer from the evolved giant companion (Andersen et al. 1988).

Previous O–C analyses by Guinan & Tomczyk (1979) indicate that the orbital period of SX Cas is not strictly constant, while polarimetric modeling by Piirola et al. (2006) constrained the geometry of the electron-scattering circumstellar envelope around the primary component through UBVRI observations. These results collectively suggest that SX Cas is a strongly interacting binary system undergoing active mass transfer and exhibiting complex circumstellar structures. However, the physical origin of its period variability remains uncertain.

A particularly powerful framework for interpreting such systems is provided by Double Periodic Variables (DPVs), which exhibit both an orbital period and a longer photometric cycle typically associated with accretion-disk dynamics. The photometric behavior of SX Cas — including its long orbital period, evidence for a massive accretion disk, and indications of variability beyond the orbital timescale — is consistent with that observed in DPV systems. However, its classification as a DPV remains uncertain and requires further observational confirmation.

[1] https://simbad.cds.unistra.fr/simbad/

Why focus on SX Cas? First, its long orbital period and clear evidence of a massive accretion disk make it a promising candidate for comparison with known DPV systems. In particular, it shares some characteristics with interacting binaries such as RX Cas (Mennickent et al. 2022) and AU Mon (Celedón et al. 2025), which exhibit complex variability patterns. At the same time, SX Cas appears to display orbital-period variability, a relatively uncommon feature among well-characterized DPVs.

Second, despite its astrophysical relevance, SX Cas has not been the subject of a comprehensive study in nearly two decades, since the polarimetric analysis by Piirola et al. (2006). During this period, a large volume of high-cadence photometric data has become available through modern surveys, yet remains largely unexplored for this system. The combination of these modern datasets with archival observations spanning more than a century provides a unique opportunity to investigate long-term variability on unprecedented timescales.

Third, identifying a long photometric cycle or disk-morphology changes in SX Cas would contribute to extending the DPV population toward longer-period and more evolved systems. Such an extension would provide valuable constraints on the role of mass transfer and disk evolution in shaping long-term variability in interacting binaries.

Accordingly, this work aims to: (a) compile and update all available photometry for SX Cas, encompassing ground-based observations, space-based data, and historical archives; (b) constrain the orbital period variability and derive updated system parameters; and (c) search for orbital-morphology variability and a possible long photometric cycle analogous to those observed in DPVs, using period-analysis tools (PDM, Stellingwerf 1978; GLS, Zechmeister & Kürster 2009; WWZ, Foster 1996) and light-curve modeling via an optimized simplex algorithm (Djurasevic 1992; Djurašević 1996; Djurašević et al. 2008).

To guide this investigation, we formulate the following working hypotheses:

- **Primary hypothesis**: SX Cas exhibits a long-term photometric cycle broadly analogous to those observed in DPVs. However, given the current observational limitations, the presence, stability, and physical origin of such a cycle cannot be established a priori.
- **Secondary hypotheses**: *Disk dynamics* — Any long photometric cycle, if

present, may be associated with temporal variations in the structure of the accretion disk, including changes in its radius, thickness, and temperature distribution. *Orbital period modulation* — The complex, non-parabolic variations observed in the O–C diagram may be consistent with magnetic activity cycles in the donor star (Applegate mechanism; Applegate 1992) and/or variations in the mass transfer rate, although alternative explanations (e.g., third-body effects) cannot be excluded.

This thesis is structured as follows: Chapter 2 presents the datasets used; Chapter 3 describes the methods; Chapter 4 presents the results; Chapter 5 discusses their interpretation; and Chapter 6 summarizes the main conclusions.

Chapter 2

Data

In this chapter, we present the different datasets from which the photometric data were collected, along with the relevant caveats associated with each. These data were compiled from several previously published studies and publicly available databases. The overall collection includes measurements in different photometric passbands—specifically V, B, and I_c—as well as historical visual-magnitude records from early archives. Despite this multi-band coverage, V-band data serve as the primary dataset for the bulk of the analysis; the remaining bands are employed mainly to determine minimum-light times (primary eclipses) and to corroborate the main results via periodogram analyses.

2.1 On Visual Photometric Data

It is important to note that visual magnitudes, although numerically similar to V-band magnitudes, are not identical quantities and cannot be treated interchangeably without correction. Accordingly, when incorporating both types of observations into a unified analysis, visual magnitudes must be shifted to match the corresponding V-band flux scale.

In this study, visual measurements were shifted to match the mean magnitude of the KWS dataset (Section 2.3.6). This mean value was calculated as the simple arithmetic average of all V-band observations in the dataset. This correction must be kept in mind when interpreting results derived from the full composite light curve, particularly regarding absolute eclipse depths or steady-state temperatures.

Reference	Band	ΔHJD - 2400000	N	Magnitude (mag)	σ (mag)	Label
Luizet (1909)	Visual	17925-18370	98	8.862	NA	A
Dugan (1933)	Visual	22628-26743	508	8.195	NA	B
Shao (1967)	V	37649-38384	80	9.125	0.009	C
Shao (1967)	B	37649-38384	80	9.904	0.0245	D
Koch (1972)	V	38711-39671	517	9.089	NA	E
Koch (1972)	B	38711-39671	507	9.808	NA	F
Piirola et al. (2006)	V	44867-46000	603	9.197	NA	G
Piirola et al. (2006)	B	44867-46000	603	10.025	NA	H

Table 2.2.1: Details of the datasets collected from previously published articles. *First column:* Article from which the data were obtained; *second column:* passband in which data were stored (in this work); *third column:* time range of the dataset, in HJD−2400000; *fourth column:* number of data points; *fifth column:* mean magnitude of the dataset, in magnitudes; *sixth column:* average data point uncertainty, in magnitudes. See text for a description of the processing applied to each dataset.

However, it is crucial to emphasize that a simple zero-point magnitude shift does not alter the timing of the eclipse minima, nor does it affect the fundamental frequencies extracted by periodogram analyses (PDM, GLS, WWZ). Therefore, this homogenization process is perfectly adequate and robust for the primary timing and periodicity objectives of this study.

2.2 Data from Previously Published Articles

A review of the published literature on this system revealed photometric observations dating back over 100 years. These historical data are invaluable because they allow us to substantially extend the temporal baseline of the analysis. Below we describe how each dataset extracted from the published literature was processed and stored for this work. Table 2.2.1 summarizes the properties of these datasets.

2.2.1 Luizet (1909)

These data were obtained from photographic plate observations. The brightness values reported by Luizet (1909) were not expressed in magnitudes; instead, they were given in units of degrees depicting the use of the Argelander method for brightness determination (see Fig. 2.2.1 for an example). Inspection of the

Dates.		L.	Δt.
1907.	h m	deg	j
Déc. 16...	9.21	11,9	15,73
17...	9.23	8,9	16,73
19...	9.11	11,9	18,72
20...	9.20	13,2	19,73
23...	6.25	16,1	22,61
23...	9. 0	14,4	22,72

Figure 2.2.1: Snapshot of the table presented in Luizet (1909). *First column:* time of observation; *second column:* brightness of the system, measured in degrees; *third column:* phase of each observation within the orbital cycle used to compute the light curve.

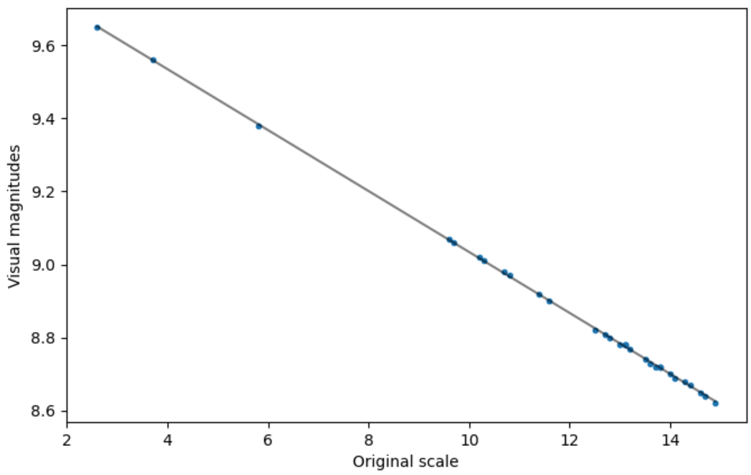

Figure 2.2.2: Data presented in Shapley (1915) for the computed light curve. A linear fit was applied to convert from the original brightness scale to visual magnitudes (Eq. 2.2.1), where D is the measurement in the original scale (degrees) and m is the resulting visual magnitude.

citations in that paper led us to Shapley (1915), in which the authors presented the computed light curve in visual magnitudes. By comparing both sources, a linear transformation was established to convert the original units to visual magnitudes (see Fig. 2.2.2):

$$m = -0.083D + 9.87 \tag{2.2.1}$$

where D denotes the measurement in the original unit of degrees.

After converting the brightness values to visual magnitudes, the observation times were transformed to Heliocentric Julian Date (HJD), applying a correction for the difference in the Earth's position relative to the Sun. The resulting dataset contains $N = 98$ data points. No brightness error estimates are available for this dataset, as the source paper did not provide uncertainties.

2.2.2 Dugan (1933)

These data were obtained through differential photometry (comparing the brightness of the system with a constant-luminosity comparisson star) and recorded in visual magnitudes. The comparison star used was BD+53°14, which has a reported visual magnitude of 9.5 in the Bonner Durchmusterung catalog (Argelander 1903). Observation times were already expressed in HJD. No error estimates were provided. After adding the magnitude of BD+53°14 to the differential measurements, we obtained a light curve containing $N = 508$ data points.

2.2.3 Shao (1967)

These data were obtained through differential photometry in the V, B, and U passbands. The comparison star used was BD +54°0011, which according to the SIMBAD database[1] has $B = 9.39 \pm 0.02$ and $V = 8.64 \pm 0.01$. Because U-band magnitudes for BD +54°0011 were not available, U-band observations were not included in this study. Observation times are measured in HJD. The internal probable error of a single measurement is ± 0.008 in ΔV and ± 0.010 in $\Delta(B - V)$. After adding the magnitude of the comparison star to each differential measurement, we obtained V and B light curves, each containing $N = 80$ data points. The typical uncertainty per measurement is ± 0.009 in V and ± 0.0245 in B.

2.2.4 Koch (1972)

These data were collected as part of a multi-observer UBV photometric campaign. Because observing capabilities and local conditions varied among contributors, the dataset exhibits slight non-uniformity in quality. Residual scale errors in V, $B - V$, and $U - B$ through the secondary eclipse were estimated to be smaller than 0.01 mag; however, these errors cannot be reliably quantified throughout the

[1] https://simbad.cds.unistra.fr/simbad

primary eclipse due to the sparse sampling of the data. No formal error estimates were provided in the original study. After compiling these records, we obtained a V-band light curve containing $N = 517$ data points and a B-band light curve containing $N = 507$ data points. The U-band observations were excluded from the analysis; as this is the only available dataset for that passband and is limited to a brief temporal interval, it does not provide the coverage required to support the long-term photometric analysis presented in this study.

2.2.5 Piirola et al. (2006)

This is the most recent study to examine SX Cas directly and in detail, published almost 20 years ago. It consists of a UBVRI polarimetric analysis of the system, supplemented by differential photometry obtained with the CRAO 1.25 m telescope. The comparison star is BD +54°0011, which, as noted above, has $B = 9.39 \pm 0.02$ and $V = 8.64 \pm 0.01$. Observation times were provided in Julian Date (JD) and were converted to HJD using the `helio_jd` function of the PyAstronomy package in Python, taking into account the system coordinates. No photometric error estimates were given in the source paper. After applying the comparison-star magnitude to each differential measurement, we obtained V and B light curves, each containing $N = 603$ data points. It is worth to note here, that all the modern survey data acquired after this date (see Section 2.3) represent entirely unexplored territory for understanding the system's long-term evolution.

2.3 Data from Publicly Available Surveys

Modern automated sky surveys make it possible to accumulate large photometric datasets for the study of variable objects. A number of publicly available surveys provide long-baseline time-series photometry for eclipsing binaries and other periodic variables, enabling analyses of high statistical significance. Below we describe each of the surveys from which data were extracted, along with the specific considerations applicable to each.

2.3.1 Hipparcos

The Hipparcos Catalog is one of the two major stellar astrometric catalogs produced by ESA's Hipparcos space mission (Perryman et al. 1997). Data for

Survey	Band	ΔHJD - 2400000	N	Magnitude (mag)	σ (mag)	Reference	Label
Hipparcos	V	47882-49014	175	9.019	0.026	Perryman et al. (1997)	I
Hipparcos	B	47882-49014	175	9.809	0.032	Perryman et al. (1997)	J
NSVS	V	51553-51593	73	9.020	0.011	Woźniak et al. (2004)	K
IOMC	V	52639-59605	542	8.998	0.012	Mas-Hesse et al. (2003)	L
APASS	V	55882-56259	6	9.047	0.001	Henden et al. (2009, 2015)	M
APASS	B	55882-56259	6	9.645	0.001	Henden et al. (2009, 2015)	N
AAVSO	V	57940-58355	127	9.023	0.033	Kloppenborg (2023)	O
AAVSO	TG	56873-58355	59	9.081	0.057	Kloppenborg (2023)	P
KWS	V	55777-60634	2167	9.006	0.020	Maehara (2014)	Q
KWS	B	57135-57557	73	9.677	0.092	Maehara (2014)	R
KWS	I_c	56429-60634	1342	7.965	0.022	Maehara (2014)	S

Table 2.3.1: Details of the datasets obtained from publicly available surveys. *First column:* name of the survey; *second column:* passband in which data were stored (in this work); *third column:* time range of the dataset, in HJD−2400000; *fourth column:* number of data points; *fifth column:* mean magnitude of the dataset, in magnitudes; *sixth column:* average data point uncertainty, in magnitudes. See text for a description of the processing applied to each dataset.

SX Cas were retrieved from the Hipparcos catalog via the VizieR online database[2]. Brightnesses are measured in the Hipparcos H_p passband. The H_p magnitudes were transformed to V-band magnitudes using the equations provided by Harmanec (1998), adopting a color index $B - V = 0.79$ from SIMBAD[3] and neglecting the third-order coefficient multiplying $U - B$. This approximation neglects the $B - V$ variability but allows a first-order approximation to the V and B light curves. An error of 0.03 in $B - V$ would result in an uncertainty of 0.01 in V and less than 0.02 in B, and the dependence on $U - B$ is negligibly weak (Harmanec 1998). Observation times were expressed in JD and were converted to HJD using the same method as for the Piirola et al. (2006) data. After this process, we obtained V and B light curves with $N = 175$ each.

2.3.2 Northern Sky Variability Survey

The Northern Sky Variability Survey (NSVS; Woźniak et al. 2004) is a temporal record of the sky covering the optical magnitude range $V \approx 8$–15.5. It was conducted during the first-generation Robotic Optical Transient Search Experiment (ROTSE-I) using a robotic system of four co-mounted unfiltered telephoto lenses equipped with CCD cameras. The public repository where the data were hosted

[2] https://vizier.cds.unistra.fr/
[3] https://simbad.cds.unistra.fr/simbad

has since been shut down; the data used in this study were provided by the supervisor of this work, Dr. Ronald Mennickent. Observation times were measured in JD and were converted to HJD using the same method as for the Piirola et al. (2006) data. We obtained a V-band light curve with $N = 73$.

2.3.3 Optical Monitoring Camera on Board the INTEGRAL Satellite

The Optical Monitoring Camera (OMC; Mas-Hesse et al. 2003) on board the INTEGRAL satellite provides measurements for sources brighter than $V \sim 18$ (Domingo et al. 2010). Data for SX Cas were retrieved from the OMC science archive at CAB[4]. Observation times are expressed in Barycentric Julian Date, which is JD corrected for differences in the Earth's position relative to the Solar system barycenter. It differs from HJD by approximately ± 4 s. In the context of this work, this difference is negligible because the timescales of the system are on the order of tens of days. We obtained a V-band light curve with $N = 542$.

2.3.4 The AAVSO Photometric All-Sky Survey

The AAVSO Photometric All-Sky Survey (APASS) is a survey using twin astrographs with CCD cameras covering the entire sky in five bandpasses: Johnson B and V, along with Sloan g', r', and i' (Henden et al. 2009, 2015). APASS epoch photometry was accessed through a mirror on the AAVSO Variable Star Index (VSX) page for SX Cas[5]. Observation times were measured in HJD. We obtained light curves in V and B, each with $N = 6$. Data in the g', r', and i' bands were discarded, as no additional observations in those passbands were available and the number of points was insufficient for a meaningful analysis ($N < 10$). Given that only $N = 6$ data points were available, this dataset was insufficient to perform any standalone periodogram or structural modeling, but the individual measurements were kept in the composite historical dataset for completeness.

[4] https://sdc.cab.inta-csic.es/omc/
[5] https://www.aavso.org/vsx/

2.3.5 Observations of the American Association of Variable Star Observers

We also considered the archival observations of the American Association of Variable Star Observers (AAVSO; Kloppenborg 2023). These observations were submitted to the AAVSO database by different observers worldwide. Visual, Tri-color Green (TG), and V-band observations were available. Only the V-band light curve was included in the analysis, since the visual observations were very few and their time span was already covered by other datasets. TG observations were used solely to determine times of minimum light. In addition, 29 observations made in 2006 (provided by a single observer) were found to be systematically offset to significantly fainter magnitudes relative to all other measurements and were therefore discarded. Observation times were measured in JD and converted to HJD. The resulting V-band light curve contains $N = 127$ data points.

2.3.6 Kamogata Kiso Kyoto Wide-Field Survey

The Kamogata Kiso Kyoto wide-field survey (KWS; Maehara 2014) is an automated survey for variable stars and transient objects, measuring brightnesses in the B, V, and Cousins I_c passbands. Data for SX Cas were retrieved from the KWS online archive[6]. Observation times were expressed in JD and converted to HJD. No KWS data were discarded. We obtained V, B, and I_c light curves containing $N = 2167$, 73, and 1342 data points, respectively. It is important to note that this survey is still ongoing, and therefore data acquired after the analysis cutoff date are not included in this work.

2.3.7 Discarded Surveys

Data for SX Cas were found in several surveys that were ultimately excluded from the analysis due to quality issues or incompatibility with the rest of the dataset. Specifically:

- *All-Sky Automated Survey for Supernovae* (ASAS-SN): ASAS-SN is an automated program designed to detect supernovae and other transient events, providing photometry in the V and g bands (Shappee et al. 2014; Kochanek

[6] http://kws.cetus-net.org/~maehara/VSdata.py

et al. 2017). When examining the SX Cas data, we found substantially higher scatter compared to contemporaneous data from KWS (see Section 2.3.6), making it difficult to detect even the orbital periodicity. Furthermore, the data retrieval page included a warning indicating that the measurements may be affected by saturation. For these reasons, ASAS-SN data were not used in this work.

- *SuperWASP*: The SuperWASP (Wide Angle Search for Planets) project is an international photometric survey designed primarily to detect transiting exoplanets (Pollacco et al. 2006). The available SX Cas data were recorded in the SuperWASP broadband SW filter, which is considerably wider than the standard Johnson V passband used in this study (see Figure 3 of Pollacco et al. (2006)). In addition, the photometric uncertainties were too large relative to those of the other surveys included here. For these reasons, SuperWASP data were also excluded.

2.4 The Light Curve

Combining all the datasets described above, we constructed B, V, and I_c light curves for SX Cas. Figures 2.4.1 and 2.4.3 provide an overall view of the complete and phase-folded light curves, respectively. As noted above, the analysis is conducted primarily in the V band (Chapter 4). The temporal distribution of the V-band data is shown in Fig. 2.4.2. The B-band light curve is used exclusively to estimate times of primary minimum, while the I_c light curve is used for period determination (both orbital and the possible long cycle) and times of minimum light.

The light curves reveal a clear periodicity near $P_{\rm orb} \sim 36.56$ d. For the purpose of this visual inspection (Fig. 2.4.3), the data were phase-folded using a period of $P_{\rm orb} = 36.566$ d. This specific value is consistent with the orbital period derived later in this work from the extensive KWS dataset ($P_{\rm orb} = 36.566 \pm 0.012$ d; see Section 4.3.1), which was determined using established literature values as a starting reference. In general, all datasets show consistent phase-folded behavior at this period, with the exception of some KWS measurements that show slightly increased scatter around the phased light curve. Additionally, as discussed in Chapter 4, the light curves exhibit morphological changes between epochs, together

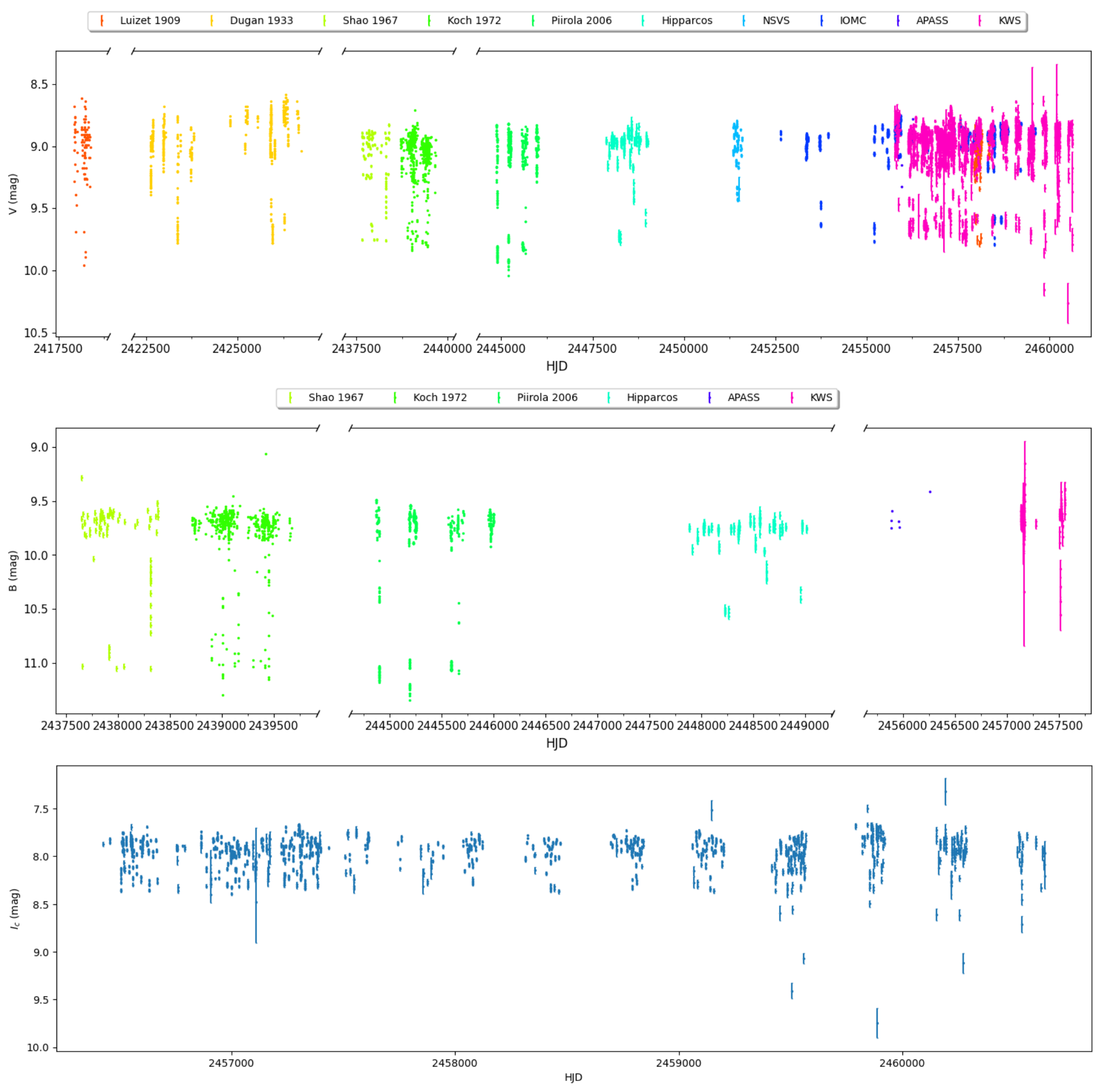

Figure 2.4.1: Light curves constructed with the datasets presented in this chapter. *Top:* V-band light curve; *middle:* B-band light curve; *bottom:* I_c-band light curve constructed with data from KWS.

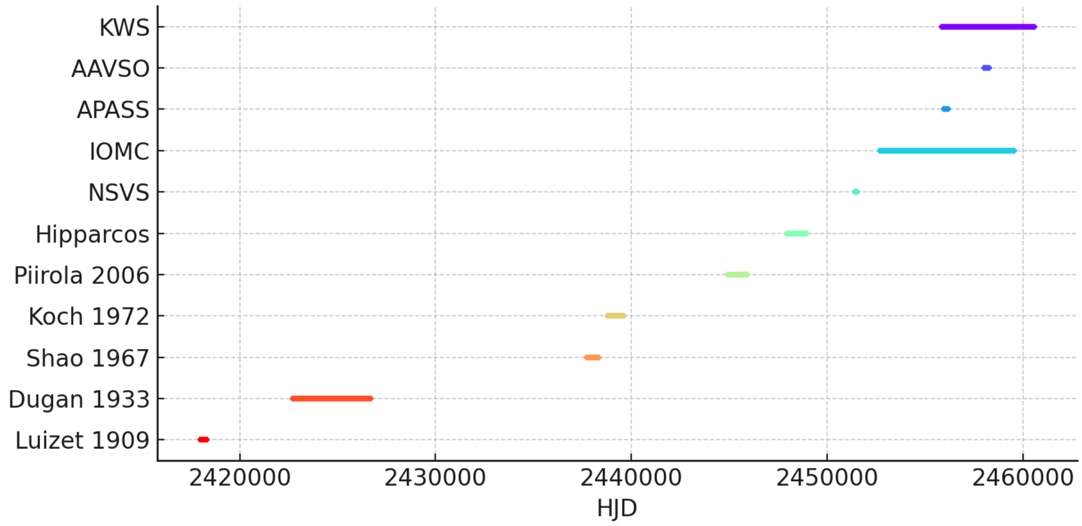

Figure 2.4.2: Temporal distribution of the V-band datasets.

with shifts in the observed times of primary minimum.

2.4.1 On Data Homogenization and Systematic Errors

When combining all the datasets, and given that all measurements were made in the V band (excluding visual data), the datasets were concatenated directly without applying any relative zero-point shifts, with the exception of the visual data, which were shifted to the mean magnitude of the KWS dataset. Two main sources of systematic error are present: (a) small zero-point offsets between datasets, which could introduce spurious signals in the period analysis; and (b) differences in the timing of eclipse minima arising from the different geographic locations of the observing sites. Since the orbital period is much longer than the light-travel time differences involved, the latter effect is negligible. Finally, it should be noted that filter transformations (e.g., from visual to V, or from the Hipparcos H_p to V) also introduce small systematic errors into the analysis, as discussed above.

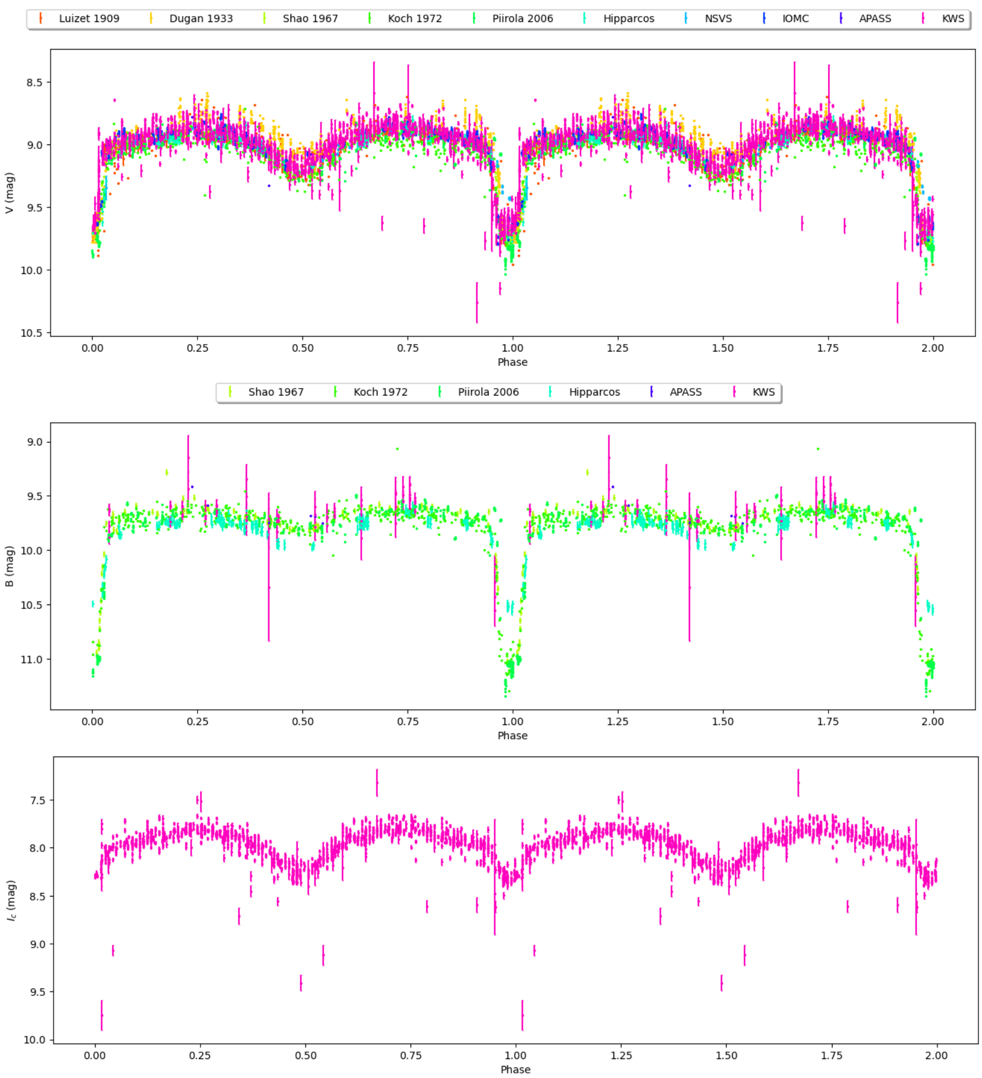

Figure 2.4.3: Same as Fig. 2.4.1, but phase-folded with the orbital period $P_{\mathrm{orb}} = 36.566 \pm 0.012$ d and a reference epoch $T_0 = 2417471.5$ HJD. *Top:* V-band light curve; *middle:* B-band light curve; *bottom:* I_c-band light curve constructed with KWS data.

Chapter 3

Methodology

3.1 Initial Inspection of Light Curves

Prior to any quantitative analysis, it is standard practice to visually inspect the datasets. Visual inspection is the first step in identifying phenomena that affect the characteristics of the light curves. In this sense, we carried out several visual inspections of the datasets and found the following:

3.1.1 Periodicity

Although this may seem like a trivial step (especially given that we are working with an eclipsing binary), visually inspecting the data to estimate the period is a necessary part of the analysis. If a periodic pattern cannot be identified by visual inspection, it is unlikely that any automated computational method will detect it reliably. In fact, without a preliminary period estimate, automated methods may return artifacts of the dataset — such as spurious periods caused by the observing cadence. This concern becomes especially important when searching for previously unreported periodicities, where spurious signals can easily be mistaken for genuine ones. As shown in Fig. 2.4.3, the system clearly exhibits an orbital period of approximately $P_{\rm orb} \sim 36.56$ d. In addition to this known period, we suspect that the light curves may also contain a longer secondary periodicity ($P_{\rm long}$). This longer cycle becomes more apparent in the more recent data, which cover a significantly wider temporal window. In the KWS data, a wave-like modulation is apparent in both the V and I_c bands, with a characteristic timescale

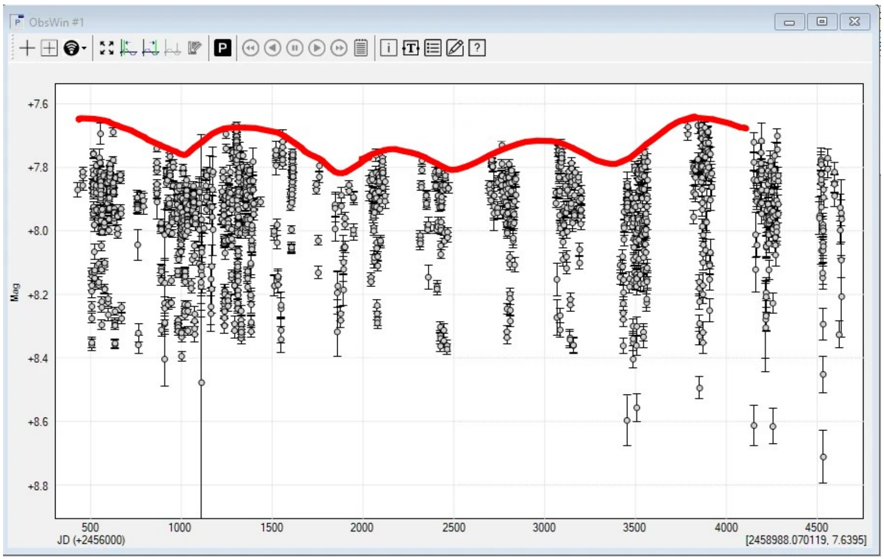

Figure 3.1.1: KWS light curve in the V band. An illustrative trendline is drawn over the data to highlight the possible presence of the long cycle P_{long}, with a characteristic timescale around $P_{\mathrm{long}} \sim 750$–$850$ d.

of approximately $P_{\mathrm{long}} \sim 750$–$850$ d (see Fig. 3.1.1).

3.1.2 Orbital Period Variation

When inspecting the phase-folded light curves of the system (Fig. 2.4.3), we noticed that the orbital phase ϕ at which the primary eclipse occurs shifts slightly and is not strictly centered at ϕ =0.0 or 1.0 across all datasets. If the orbital period were constant, the primary eclipse would consistently appear at $\phi = 0$ or $\phi = 1$. However, in our case, the primary eclipse in more recent datasets appears slightly shifted to the left of $\phi = 1$ compared to older data. This could indicate either (a) that the period reported in the literature is not sufficiently precise, or (b) that the system is undergoing a gradual period variation over time, driven by some physical process that causes the orbital period to change secularly.

3.1.3 Morphological Changes in the Light Curves

A comparison of the light curves from different datasets reveals systematic shape differences that cannot be attributed solely to period uncertainties. In particular, the shapes of the quadratures — when the system is out of eclipse — vary significantly between datasets (see Fig. 3.1.2). Such morphological variations likely reflect genuine physical changes within the system, such as structural

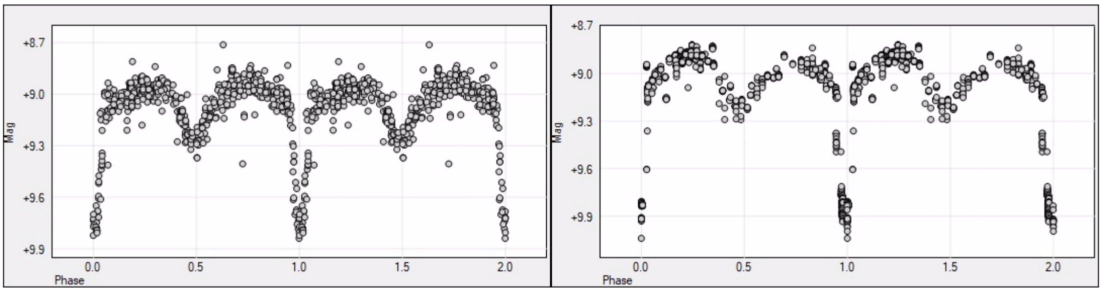

Figure 3.1.2: Phase-folded light curves from Koch (1972) (left) and Piirola et al. (2006) (right) in the V band. Morphological differences are evident: in the right panel, the first quadrature is brighter, whereas in the left panel, the second quadrature is brighter. The asymmetry between quadratures is also more pronounced in the right panel.

evolution of the accretion disk or the development of stellar and disk spots.

Furthermore, a visual inspection of the multi-band phase-folded light curves (see Fig. 2.4.3) reveals a distinct chromatic dependence: the depth of the primary eclipse decreases progressively at longer wavelengths (passing from the B band to V and then to I_c). This behavior provides direct observational evidence that the component being eclipsed at phase $\phi = 0.0$ (the primary) is substantially hotter than the occulting star, which is fully consistent with the established stellar temperatures of the system.

3.2 Periodograms

Periodograms are tools that apply mathematical or statistical methods (e.g., Fourier or variance analysis) to light curves to detect periodic signals. In this work, all periodograms were computed using the *Light Curve and Period Analysis Software* (PERANSO; Paunzen & Vanmunster 2016). Period uncertainties were estimated using the method implemented in PERANSO, which employs a Monte Carlo bootstrap approach: the observed data are randomly resampled with replacement over a large number of iterations, and the periodogram is recomputed for each realization. The resulting distribution of best-fit periods yields the 1σ uncertainty quoted throughout this work.

3.2.1 Phase Dispersion Minimization

Phase Dispersion Minimization (PDM; Stellingwerf 1978) is a technique that folds observational data over a range of trial frequencies. For each trial frequency, the phase interval $(0, 1)$ is divided into bins, and the variance within each bin is computed to quantify the scatter around the mean light curve. The PDM statistic is then obtained by dividing the total variance of the binned data by the variance of the original (unbinned) dataset. This process is repeated for all trial frequencies, and the frequency with the lowest PDM statistic corresponds to the most likely true period. The PDM method was employed to estimate the orbital period of the system, since the time span of the light curves covers hundreds of orbital cycles, producing well-sampled phase-folded light curves and reliable results. The test period range was set to $32 < P < 40$ d with a total of 5000 frequency divisions. The remaining parameters — number of bins ($N_b = 5$) and bin coverage ($N_c = 2$) — were left at their default values.

3.2.2 Generalized Lomb–Scargle

The Lomb–Scargle periodogram transforms an unevenly sampled time series into a power spectrum (Lomb 1976; Scargle 1982). The Generalized Lomb–Scargle (GLS) variant accounts for photometric uncertainties and includes a constant offset term in the fitted sinusoid (Zechmeister & Kürster 2009). GLS was employed primarily to search for the presence of a possible long-term cycle. Compared to PDM, GLS is more sensitive to long-period signals, especially when phase coverage is incomplete — as is inevitably the case for very long periods. The test period range was set to $300 < P < 1200$ d, with 5000 frequency divisions.

3.2.3 Weighted Wavelet Z-Transform

The Weighted Wavelet Z-transform (WWZ) method combines time and frequency analysis to reveal how periodicities evolve over time (Foster 1996). Unlike classical period analysis methods, WWZ produces a two-dimensional time–frequency representation in which the color scale encodes the WWZ power at each time and frequency. This makes WWZ particularly effective for detecting time-dependent period variations and for assessing the temporal stability of a detected signal.

WWZ fits a sinusoidal wavelet modulated by a Gaussian window function.

Observations near the center of the window receive the highest weights, and the window slides across the dataset to produce the time–frequency map. This method is especially useful for identifying period variations or the evolution of long-term cycles. In our analysis, we explored periods between 300 and 1200 d. The decay constant and time-step parameters, which control the wavelet window width, were kept at their default values (0.001 and 50, respectively).

3.2.4 Aliasing

When analyzing periodic signals, it is important to recognize the presence of false or "alias" periods, which arise from the sampling pattern of the observations. One way to identify such spurious signals is by examining the *spectral window* of the dataset — a Fourier power spectrum constructed under the assumption of constant brightness — which reveals periodicities introduced purely by the observational cadence. In this work, the spectral windows of the KWS V and I_c datasets were computed and inspected prior to interpreting the GLS periodograms. The dominant alias structures in both bands arise from the one-year seasonal gap (at $P \approx 365$ d and its harmonics at $\sim$183, $\sim$730 d) and from the orbital period itself ($P_{\rm orb} \approx 36.57$ d) together with its window sidelobes.

3.3 Times of Minimum Light

Because the individual light-curve segments are often too sparsely sampled to reliably define the full eclipse shape within a single cycle, standard methods such as parabolic or polynomial fitting could not be consistently applied to determine the times of minima. Instead, we adopted a threshold-based approach (e.g. Mennickent et al. (2022)) in which a brightness cutoff was defined for each dataset to identify observations corresponding to the primary eclipse minimum.

The adopted thresholds were determined visually for each dataset and are listed in Table 3.3.1. While this procedure is inherently approximate, it provides a consistent and reproducible criterion for extracting minima across heterogeneous datasets with widely varying photometric precision and cadence. Datasets M and N were excluded due to insufficient data coverage, while dataset R was omitted because of its large observational uncertainties. For dataset S, the phase range was restricted to the vicinity of $\phi = 0$ and $\phi = 1$, since the primary and secondary

Label	Threshold (mag)	Label	Threshold (mag)
A	9.6	S	8.3
B	8.8	Q	9.7
C	9.75	P	9.6
D	11.0	O	9.5
E	9.75	L	9.6
F	11.0	K	9.3
G	9.65	I	9.75
H	11.0		

Table 3.3.1: Brightness thresholds used to identify primary eclipse minima in each dataset. All values were determined visually.

eclipses have comparable depths and could otherwise be misidentified.

We emphasize that no formal uncertainty estimates were assigned to the derived times of minimum light. Consequently, all timings were treated equally in subsequent least-squares analyses. This approach implicitly assumes that the individual timing uncertainties are small compared to the long-term variations being investigated; however, we caution that this is an approximation. The resulting O–C analysis should therefore be interpreted in terms of global, long-term trends rather than precise cycle-to-cycle variations.

Using this threshold-based method, we derived a total of 399 new primary eclipse timings from our datasets. In addition, we included 66 eclipse timings from the Lichtenknecker Database of the Berliner Arbeitsgemeinschaft für Veränderliche Sterne (BAV)[1]. All these minima were used in the construction of the O–C diagram.

3.4 O–C Analysis

The O–C method (Observed minus Calculated) evaluates how well predicted event timings match observations (Sterken 2005). For periodic phenomena, an ephemeris can be defined as

$$T_m(E) = T_0 + PE, \tag{3.4.1}$$

[1] https://www.bav-astro.eu/index.php/veroeffentlichungen/service-for-scientists/lkdb-engl

where E is the cycle number, T_0 the reference epoch and P is the period. Deviations from this simple linear ephemeris indicate changes in the period, which may be time-dependent:

$$T_m(t) = T_0 + \int P(t)\,dt, \tag{3.4.2}$$

$$T_m(E) = T_0 + \int P(E)\,dE. \tag{3.4.3}$$

Systematic deviations in O–C diagrams can reveal trends such as cyclic variations or secular period changes, which may result from processes such as the presence of a third body, apsidal motion, or mass transfer between the binary components (Sterken 2005).

3.4.1 Linearly Changing Period

A common case occurs when the period changes linearly with time:

$$P(t) = P_r + \frac{dP}{dt}t, \tag{3.4.4}$$

$$P(E) = P_r + \frac{dP}{dt}\bar{P}E, \tag{3.4.5}$$

With P_r the real period of the system and $\bar{P}$ the mean period over time. Yielding observed timings of minima:

$$O = T_r + P_rE + \frac{1}{2}\frac{dP}{dt}\bar{P}E^2. \tag{3.4.6}$$

Where T_r the real reference epoch. Comparing this to the calculated (C) ephemeris:

$$(O - C) = (T_r - T_0) + (P_r - P)E + \frac{1}{2}\frac{dP}{dt}\bar{P}E^2. \tag{3.4.7}$$

This produces a parabolic trend in the O–C diagram (see Fig. 3.4.1). Such a trend can be fitted as:

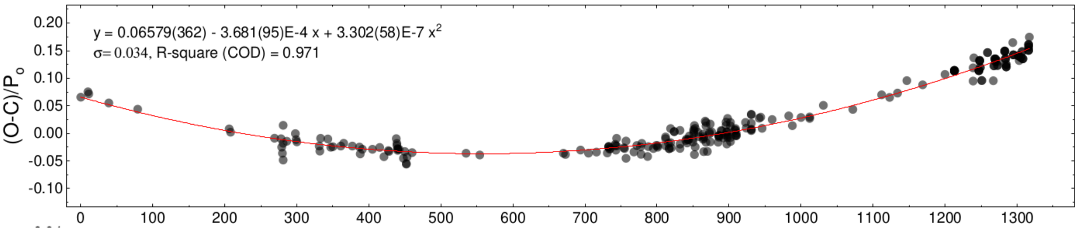

Figure 3.4.1: O–C diagram of the system RX Cas. Adapted from Mennickent et al. (2022).

$$AE^2 + BE + C = (T_r - T_0) + (P_r - P)E + \frac{1}{2}\frac{dP}{dt}\bar{P}E^2, \tag{3.4.8}$$

from which:

$$A = \frac{1}{2}\frac{dP}{dt}\bar{P}, \qquad B = P_r - P, \qquad C = T_r - T_0. \tag{3.4.9}$$

Here, A directly relates to the rate of period change. As demonstrated in numerous recent studies (e.g., de Miguel et al. 2018), the rate of period variation derived from an O–C diagram can be used to estimate the mass transfer rate of the system. According to standard close binary evolution theory (e.g., Kopal 1959), assuming conservative mass transfer (where the total mass and orbital angular momentum remain constant), the relationship between the period change $\dot{P}$ and the mass transfer rate $\dot{M}$ is given by:

$$\frac{\dot{P}}{P} = 3\dot{M}_g \left(\frac{M_g - M_d}{M_g M_d} \right), \tag{3.4.10}$$

where M_g and M_d are the masses of the gainer and donor stars, respectively, and $\dot{M}_g = -\dot{M}_d$ represents the mass transfer rate. It is essential, however, to justify the choice of the fitted function carefully — whether linear, parabolic, sinusoidal, or a combination — in order to avoid overfitting and misinterpretation. In this work, we adopt a linear ephemeris for the primary eclipses and compare it with the observed minima to construct the O–C diagram. The resulting trends are then analyzed and fitted with appropriate models.

3.5 Light Curve Analysis

Light curve analysis refers to the study of the curve's morphology — eclipse depths, durations, and quadrature shapes (i.e. the shape of the light curve outside the eclipses) — to infer the system's physical properties, such as stellar parameters, disk structure, and the presence of spots or other phenomena.

For the light curve analysis, we required a specialized approach capable of handling the complex geometry of SX Cas. Standard binary modeling codes often struggle with massive, non-steady circumprimary structures. Therefore, we utilized the LC Analysis Code developed by Dr. Gojko Djurašević[2]. This specific algorithm is mathematically optimized for solving the inverse problem in binary systems hosting optically and geometrically thick accretion disks operating in critical non-synchronous rotation regimes —precisely the physical environment of SX Cas. To mitigate the risk of the simplex algorithm converging on non-physical local minima, the parameter space exploration was tightly constrained by the fixed kinematic and geometric limits imposed by the eclipse durations.

Because the code optimizes parameters for the input light curve as a whole, thereby averaging out long-term morphological changes, we divided the composite V-band light curve into five temporal segments. Two conditions were required for segmentation:

1. Sufficient data coverage to clearly identify the light curve morphology.
2. No significant temporal gaps within a segment.

Of these, the first criterion was prioritized, as a clearly recognizable light curve shape is essential for reliable modeling.

A custom inspection code was written to define each section interactively (Fig. 3.5.1).

[2]Belgrade Observatory, gdjurasevic@aob.rs

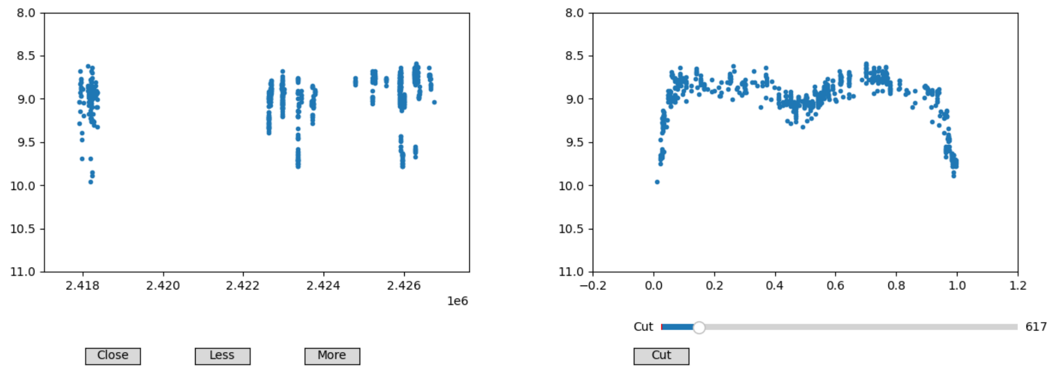

Figure 3.5.1: Example of segment selection. *Left:* raw light curve of the first segment. *Right:* phase-folded light curve of the same segment. Both selection criteria are satisfied: (1) the light curve morphology is clearly identifiable, and (2) no significant temporal gaps are present.

Chapter 4

Results

4.1 Minima Detection

We investigated the Lichtenknecker Database of the German Association of Variable Stars (BAV), which lists 66 primary eclipse timings for SX Cas. In addition to these, we derived 399 new primary eclipse timings using the methodology described in Section 3.3. Tables 4.2.1, 4.2.2, and 4.2.3 list all of these timings.

4.2 Rate of Orbital Period Change

We performed an O–C analysis of the eclipse timings (Sterken 2005) for SX Cas, adopting

$$C = \mathrm{HJD}_0 + P_0 E, \qquad O = \mathrm{HJD}_{\mathrm{min}} \tag{4.2.1}$$

where P_0 is a representative value of the orbital period P_{orb} for the entire light curve, E is the cycle number, HJD_0 is the reference primary eclipse time, and $\mathrm{HJD}_{\mathrm{min}}$ represents the observed times of minimum light. We adopt $\mathrm{HJD}_0 = 2417471.1$, a primary eclipse time reported in the Lichtenknecker Database, and $P_0 = 36.566 \pm 0.012$ d as the reference orbital period after several trials to best represent the full time span of the light curve. For $\mathrm{HJD}_{\mathrm{min}}$, we use a total of 465 eclipse minima, including both the times reported in the Lichtenknecker Database and those derived in this work.

HJD	Label	HJD	Label	HJD	Label	HJD	Label
2418202.86153	A	2437656.61500	C	2444896.34555	G	2445188.47439	G
2418238.88025	A	2437985.70900	C	2444896.34795	G	2445189.49496	G
2418238.90594	A	2438058.57100	C	2444896.35045	G	2445189.49736	G
2423358.52150	B	2438314.60000	C	2444896.35285	G	2445189.49976	G
2423358.52530	B	2437656.61500	D	2444896.35575	G	2445189.50226	G
2423358.52990	B	2437985.70900	D	2444896.35825	G	2445189.50666	G
2423358.53370	B	2438058.57100	D	2444896.36065	G	2445189.50906	G
2423358.53750	B	2438314.60000	D	2444896.36315	G	2445189.51156	G
2423358.54170	B	2439009.31370	E	2444896.42415	G	2445189.51396	G
2423358.54690	B	2439009.46200	E	2444896.42615	G	2445189.51736	G
2423358.55100	B	2439009.50200	E	2444896.42855	G	2445189.51986	G
2423358.68130	B	2439009.51600	E	2444896.43095	G	2445189.52226	G
2423358.68540	B	2439119.22540	E	2444896.43485	G	2445189.52466	G
2423358.68990	B	2439301.34320	E	2444896.43735	G	2445189.52866	G
2423358.69410	B	2439302.33620	E	2444896.43975	G	2445189.53106	G
2423359.53510	B	2439374.84530	E	2444896.44175	G	2445189.53346	G
2423359.53920	B	2439411.76390	E	2444896.44565	G	2445189.53596	G
2423359.54340	B	2439411.86840	E	2444896.44805	G	2445590.51553	G
2423359.68440	B	2439448.46900	E	2444896.45055	G	2445590.51793	G
2423359.68850	B	2439448.48500	E	2444896.45295	G	2445590.52033	G
2423359.69270	B	2439448.50400	E	2444896.45685	G	2445590.52283	G
2423359.69900	B	2438973.55510	F	2444896.45885	G	2445590.53223	G
2425954.45280	B	2439009.31370	F	2444896.46125	G	2445590.53463	G
2425954.45700	B	2439009.46200	F	2444896.46375	G	2445590.53703	G
2425954.46180	B	2439009.48300	F	2444896.46765	G	2445590.53903	G
2425954.46560	B	2439009.50200	F	2444896.47005	G	2445590.48773	G
2425954.47150	B	2439009.51600	F	2444896.47245	G	2445590.49023	G
2425954.47570	B	2439118.94830	F	2444896.47495	G	2445590.49263	G
2425954.48440	B	2439119.22540	F	2445188.43529	G	2445590.49513	G
2425954.48850	B	2439302.33620	F	2445188.43769	G	2445590.50193	G
2425954.49240	B	2439411.76390	F	2445188.44019	G	2445590.50423	G
2425954.49650	B	2439411.86840	F	2445188.44259	G	2445590.50623	G
2425954.55760	B	2439448.46900	F	2445188.44599	G	2445590.50863	G
2425954.56250	B	2439448.48500	F	2445188.44849	G	2445591.33487	G
2425954.56560	B	2439448.50400	F	2445188.45089	G	2445591.33696	G
2425954.56910	B	2444896.32165	G	2445188.45339	G	2445591.33927	G
2425954.57260	B	2444896.32405	G	2445188.45679	G	2445591.34177	G
2425954.57570	B	2444896.32645	G	2445188.45919	G	2445591.34917	G
2425954.68440	B	2444896.32895	G	2445188.46169	G	2445591.35157	G
2425954.68780	B	2444896.33385	G	2445188.46409	G	2445591.35397	G
2425954.69130	B	2444896.33625	G	2445188.46699	G	2445591.35647	G
2425954.69480	B	2444896.33875	G	2445188.46949	G	2445591.36327	G
2425954.69860	B	2444896.34065	G	2445188.47189	G	2445591.36577	G

Table 4.2.1: New photometric timings identified with minima for the main eclipse (part 1)

HJD	Label	HJD	Label	HJD	Label	HJD	Label
2445591.36817	G	2444896.32895	H	2445189.49976	H	2445591.40287	H
2445591.37017	G	2444896.33385	H	2445189.50226	H	2445591.40527	H
2445591.37357	G	2444896.33625	H	2445189.50666	H	2445591.46777	H
2445591.37597	G	2444896.33875	H	2445189.50906	H	2445591.47027	H
2445591.37847	G	2444896.34065	H	2445189.51156	H	2445591.47267	H
2445591.38087	G	2444896.34555	H	2445189.51396	H	2445591.47507	H
2445591.38767	G	2444896.34795	H	2445189.51736	H	2445591.48197	H
2445591.39017	G	2444896.34795	H	2445189.51986	H	2445591.48437	H
2445591.39257	G	2444896.35285	H	2445189.52226	H	2445591.48637	H
2445591.39507	G	2444896.35575	H	2445189.52466	H	2445591.48877	H
2445591.39797	G	2444896.35825	H	2445189.52866	H	2445591.49267	H
2445591.40037	G	2444896.36065	H	2445189.53106	H	2445591.49467	H
2445591.40287	G	2444896.36315	H	2445189.53346	H	2445591.49707	H
2445591.40527	G	2444896.42415	H	2445189.53596	H	2445591.49957	H
2445591.46777	G	2444896.42615	H	2445590.53223	H	2445591.50687	H
2445591.47027	G	2444896.42855	H	2445590.53463	H	2445591.50927	H
2445591.47267	G	2444896.43095	H	2445590.53703	H	2445591.51177	H
2445591.47507	G	2444896.43485	H	2445590.53903	H	2445591.51417	H
2445591.48197	G	2444896.43735	H	2445590.48773	H	2445591.51707	H
2445591.48437	G	2444896.43975	H	2445590.49263	H	2445591.51957	H
2445591.48637	G	2444896.44175	H	2445590.49513	H	2445591.52197	H
2445591.48877	G	2444896.44565	H	2445591.33487	H	2445591.52397	H
2445591.49267	G	2444896.44805	H	2445591.33696	H	2445591.53127	H
2445591.49467	G	2444896.45055	H	2445591.33927	H	2445591.53367	H
2445591.49707	G	2444896.45295	H	2445591.34177	H	2445591.53617	H
2445591.49957	G	2444896.45685	H	2445591.34917	H	2445591.53857	H
2445591.50687	G	2444896.45885	H	2445591.35157	H	2445664.33536	H
2445591.50927	G	2444896.46125	H	2445591.35397	H	2445664.34416	H
2445591.51177	G	2444896.46375	H	2445591.35647	H	2448260.52200	I
2445591.51417	G	2444896.46765	H	2445591.36327	H	2451442.61601	K
2445591.51707	G	2444896.47005	H	2445591.36577	H	2451442.61633	K
2445591.51957	G	2444896.47245	H	2445591.36817	H	2451442.67158	K
2445591.52197	G	2444896.47495	H	2445591.37017	H	2451442.67190	K
2445591.52397	G	2445188.43529	H	2445591.37357	H	2451478.58256	K
2445591.53127	G	2445188.43769	H	2445591.37597	H	2451478.58287	K
2445591.53367	G	2445188.44019	H	2445591.37847	H	2451478.63952	K
2445591.53617	G	2445188.44259	H	2445591.38087	H	2451478.63984	K
2445591.53857	G	2445188.44599	H	2445591.38767	H	2451513.62538	K
2445664.33536	G	2445188.44849	H	2445591.39017	H	2453744.99426	L
2445664.34416	G	2445188.45089	H	2445591.39257	H	2453745.00059	L
2444896.32165	H	2445188.45339	H	2445591.39507	H	2453745.00945	L
2444896.32405	H	2445189.49496	H	2445591.39797	H	2453745.01577	L
2444896.32645	H	2445189.49736	H	2445591.40037	H	2453745.02463	L

Table 4.2.2: New photometric timings identified with minima for the main eclipse (part 2)

HJD	Label	HJD	Label	HJD	Label	HJD	Label
2455208.10982	L	2458682.27978	L	2456999.34884	P	2457730.91241	Q
2455208.11591	L	2458682.29451	L	2456159.20209	Q	2457730.91269	Q
2455208.12446	L	2458682.30432	L	2456159.20244	Q	2457731.92483	Q
2455208.13054	L	2451442.61601	O	2456196.10154	Q	2457731.92509	Q
2455208.13909	L	2451442.61633	O	2456196.10189	Q	2457731.92697	Q
2455208.48884	L	2451442.67158	O	2456598.02248	Q	2457731.92724	Q
2455208.49517	L	2451442.67190	O	2456634.95448	Q	2459487.09655	Q
2455208.50403	L	2451478.58256	O	2457000.96117	Q	2459487.09965	Q
2455208.51035	L	2451478.58287	O	2457549.28854	Q	2459853.10064	Q
2455208.51541	L	2451478.63952	O	2457622.17313	Q	2459890.99776	Q
2458500.36946	L	2451478.63984	O	2457622.17341	Q	2460513.29620	Q
2458500.37543	L	2451513.62538	O	2457658.14089	Q	2460621.00140	Q
2458500.39939	L	2457255.56723	P	2457696.00459	Q	2460621.00175	Q
2458682.23791	L	2457219.66308	P	2457696.00487	Q		

Table 4.2.3: New photometric timings identified with minima for the main eclipse (part 3)

After comparing the observed timings of minimum light with the expected values, we constructed the O–C diagram for the system (Fig. 4.2.1). We note that no uncertainty estimates are available for the times of minimum light, which may have some impact on the subsequent results extracted from the O–C analysis.

To model the complex variations observed in the O–C diagram, we must adopt analytical models (*ansätze*) that are well-established in the literature for interacting binaries. In this work, we evaluate two main mathematical formulations.

First, we evaluate a fourth-order polynomial. In O–C analysis, higher-order polynomials are routinely employed as empirical representations of complex dynamics (Sterken 2005). Physically, a fourth-order fit can describe a time-variable rate of mass transfer (where the mass transfer rate itself is not strictly constant), or it can serve as a Taylor-series approximation for a long-period cyclic modulation whose full orbital period vastly exceeds the available observational baseline.

Second, we consider a composite function consisting of a second-order polynomial and a superimposed sinusoidal modulation. This is the standard *ansatz* widely used to represent simultaneous secular mass transfer and a cyclic mechanism, such as the Light-Travel Time Effect (LTTE) or magnetic activity cycles (e.g., Sterken 2005; Applegate 1992; Irwin 1959).

By comparing these established models, we can better interpret the underlying physical mechanisms driving the period changes in SX Cas.

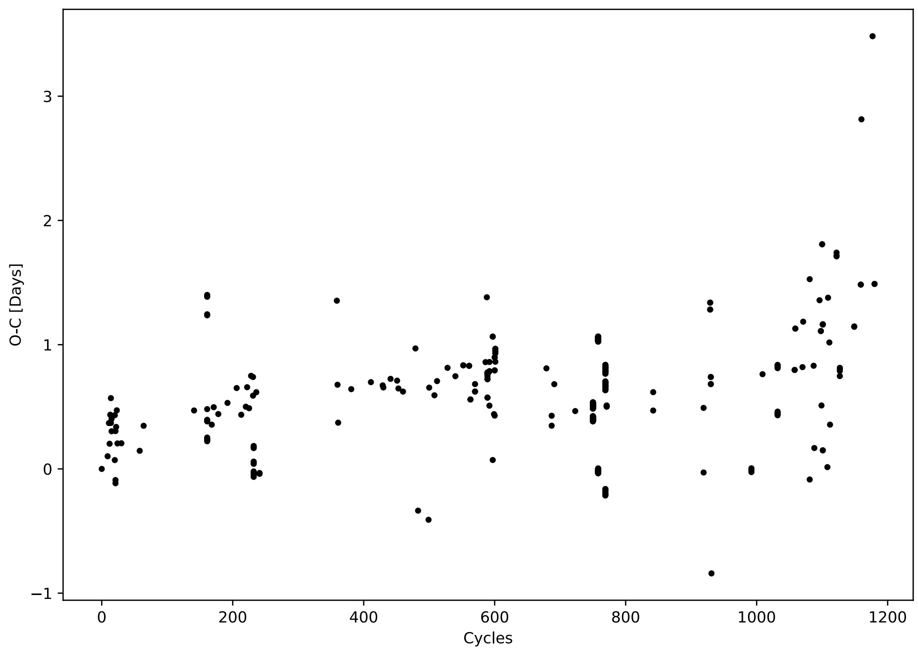

Figure 4.2.1: O–C diagram constructed using a linear reference ephemeris with $T_0 = 2417471.1$ and $P_0 = 36.566$ d, employing the compiled times of primary eclipse minima.

4.2.1 Polynomial Trend

The first model we considered was a fourth-order polynomial. We applied a fit of the form

$$O - C = AE^4 + BE^3 + CE^2 + DE + F, \tag{4.2.2}$$

where A, B, C, D, and F are the polynomial coefficients. From this we find

$$O - (\mathrm{HJD}_0 + P_0 E) = AE^4 + BE^3 + CE^2 + DE + F, \tag{4.2.3}$$
$$O = AE^4 + BE^3 + CE^2 + (D + P_0)E + (\mathrm{HJD}_0 + F). \tag{4.2.4}$$

We adopt the ansatz

$$P(t) = P_r + \left.\frac{dP}{dt}\right|_r t + \left.\frac{d^2P}{dt^2}\right|_r t^2 + \left.\frac{d^3P}{dt^3}\right|_r t^3, \tag{4.2.5}$$
$$P(E) = P_r + \left.\frac{dP}{dt}\right|_r \overline{P}E + \left.\frac{d^2P}{dt^2}\right|_r \overline{P}^2E^2 + \left.\frac{d^3P}{dt^3}\right|_r \overline{P}^3E^3, \tag{4.2.6}$$

where the period varies as a third-order polynomial in time, $\overline{P}$ is the mean period, and the derivatives of P with respect to time are constants. This leads to

$$O = T_r + P_rE + \frac{1}{2}\left.\frac{dP}{dt}\right|_r \overline{P}E^2 + \frac{1}{3}\left.\frac{d^2P}{dt^2}\right|_r \overline{P}^2E^3 + \frac{1}{4}\left.\frac{d^3P}{dt^3}\right|_r \overline{P}^3E^4. \tag{4.2.7}$$

Finally, setting $P_0 = \overline{P}$, we obtain

$$T_r = \mathrm{HJD}_0 + F, \qquad P_r = D + P_0,$$
$$\left.\frac{dP}{dt}\right|_r = \frac{2C}{P_0}, \qquad \left.\frac{d^2P}{dt^2}\right|_r = \frac{3B}{P_0^2}, \qquad \left.\frac{d^3P}{dt^3}\right|_r = \frac{4A}{P_0^3}.$$

We then applied a least-squares fit to the O–C diagram (Fig. 4.2.2). The resulting coefficients are listed in Table 4.2.4.

4.2.2 Parabolic Plus Sinusoidal Trend

The second model we examined was a combination of a parabolic trend and a sinusoidal modulation. The adopted functional form is

$$O - C = AE^2 + BE + C + K\sin(\omega E + \omega_0), \tag{4.2.8}$$

where A, B, C, K, ω, and ω_0 are constants. From this expression we obtain

$$O = AE^2 + (B + P_0)E + (C + \mathrm{HJD}_0) + K\sin(\omega E + \omega_0). \tag{4.2.9}$$

We propose the ansatz

$$P(t) = P_r + \frac{dP}{dt}t + A_0\cos(\omega_r t + \omega_{r,0}), \tag{4.2.10}$$
$$P(E) = P_r + \frac{dP}{dt}\overline{P}E + A_0\cos(\omega_r\overline{P}E + \omega_{r,0}), \tag{4.2.11}$$

where the period varies linearly with time plus a sinusoidal perturbation. Here A_0, P_r, $\frac{dP}{dt}$, ω_r, and $\omega_{r,0}$ are constants. This leads to

$$O = T_r + P_r E + \frac{1}{2}\frac{dP}{dt}\overline{P}E^2 + \frac{A_0}{\omega_r\overline{P}}\sin(\omega_r\overline{P}E + \omega_{r,0}). \tag{4.2.12}$$

Finally, taking $P_0 = \overline{P}$, we find

$$\begin{aligned} T_r &= \mathrm{HJD}_0 + C, \qquad & P_r &= B + P_0, \\ \left.\frac{dP}{dt}\right|_r &= \frac{2A}{P_0}, \qquad & \omega_r &= \frac{\omega}{P_0}, \qquad & A_0 = K\omega, \qquad & \omega_{r,0} = \omega_0. \end{aligned}$$

Considering this, we applied a least-squares fit to the data (see Fig. 4.2.3), whose parameters are listed in Table 4.2.4. Overall, both models yield similar Mean Squared Error (MSE) values and comparably low R^2. To rigorously compare these competing models beyond simple residuals, we evaluated the Akaike information

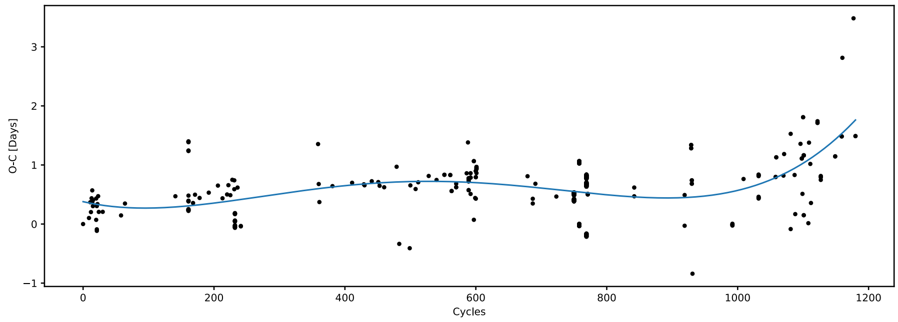

Figure 4.2.2: O–C diagram with a fourth-order polynomial fit. The coefficient of determination is $r^2 \approx 0.229$ and the mean squared error is MSE ≈ 0.154.

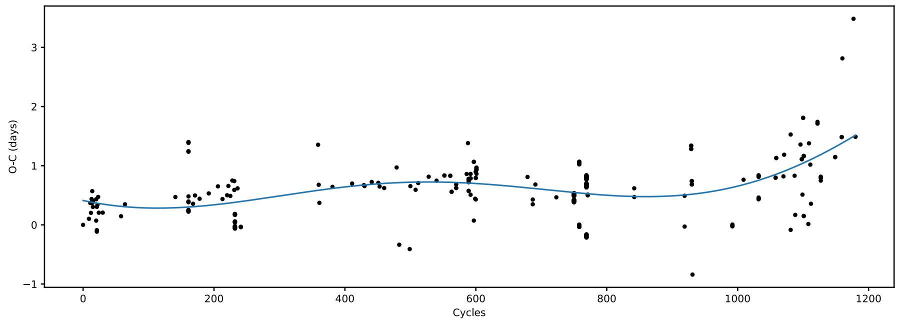

Figure 4.2.3: O–C diagram with a parabolic plus sinusoidal fit. The coefficient of determination is $r^2 \approx 0.215$ and the mean squared error is MSE ≈ 0.157.

Polynomial fit		Parabolic + sinusoidal fit	
A (days)	$(1.43 \pm 0.25)\times10^{-11}$	A (days)	$(3.2 \pm 2.9)\ \times10^{-6}$
B (days)	$(-2.89 \pm 0.57)\times10^{-8}$	B (days)	$(-3.0 \pm 3.0)\times10^{-3}$
C (days)	$(1.73 \pm 0.42)\times10^{-5}$	C (days)	0.90 ± 0.33
D (days)	$(-2.54 \pm 1.20)\times10^{-3}$	K (days)	0.50 ± 0.42
F (days)	0.38 ± 0.10	ω	$(5.8 \pm 1.8)\times10^{-3}$
		ω_0	-1.37 ± 0.92

Table 4.2.4: Coefficients of the fits described above (Sections 4.2.1 and 4.2.2).

criterion (AIC $= n\ln(\text{MSE}) + 2k$), which penalizes for overfitting based on the number of free parameters ($k = 5$ for the fourth-order polynomial vs. $k = 6$ for the parabolic-plus-sinusoidal model). Using the reported MSE values and $n = 465$ data points, we obtain $\text{AIC}_{\text{poly}} \approx -859.9$ and $\text{AIC}_{\text{par+sin}} \approx -849.0$, i.e. $\Delta\text{AIC} \approx 11$. By conventional thresholds, this formally favors the fourth-order polynomial in a purely empirical sense; however, given the sample size, this comparison is highly sensitive to the precision of the reported MSE values, and we do not regard it as decisive on its own. In this context, a high R^2 (or an AIC preference driven purely by residual minimization) would itself be suspicious. Interacting binaries with active mass transfer and convective donors are known to exhibit stochastic, short-timescale period fluctuations superimposed on secular trends — a behavior well-documented in analogous systems such as RX Cas (Mennickent et al. 2022), SW Cyg, and RR Dra (Qian et al. 2002). The O–C residuals in these systems are typically dominated by intrinsic "red noise" arising from these stochastic mass-transfer fluctuations and magnetic activity cycles (Applegate 1992). Furthermore, the 399 eclipse timings derived in this work were obtained via a brightness threshold method applied to heterogeneous datasets spanning over a century, which naturally introduces non-Gaussian scatter. Any smooth analytical model achieving an R^2 approaching unity in such a system would inevitably be overfitting this stochastic noise rather than capturing the underlying secular dynamics. Therefore, the appropriate criterion for evaluating these O–C fits is not simply a residual-based statistic such as R^2 or AIC, but whether the fitted function correctly identifies the dominant long-term trend and offers a physically plausible justification. From this perspective, the parabolic-plus-sinusoidal fit provides a much stronger foundation. In this composite model, each mathematical term maps directly to a distinct, well-documented physical mechanism: the parabolic component represents a steady secular mass transfer between the binary components, while the sinusoidal term reflects a strictly periodic perturbation, such as the Light-Travel Time Effect (LTTE) or magnetic activity cycles (the Applegate mechanism). Conversely, while the fourth-order polynomial provides a flexible empirical fit, its higher-order terms (E^3 and E^4) imply a continuously accelerating or decelerating mass transfer rate. Justifying such a smooth, long-term variation in the mass transfer dynamics is physically challenging without invoking highly complex and unconstrained mass-loss scenarios. Consequently, we favor the parabolic-plus-sinusoidal interpretation as the more physically meaningful representation of the system's long-term global dynamics. However, as a localized Taylor expansion, the polynomial derivative provides a robust empirical tool for estimating the instantaneous, current-epoch period change rate (as discussed further in Section 5.1.1). It is critical to address the statistical implications of utilizing unweighted least-squares fits in our O–C analysis. Because strict formal uncertainties could not be systematically derived for the historical visual minima, all data points were treated with equal statistical weight. Consequently, the derived parameters — particularly the higher-order coefficients in the polynomial fit — must be interpreted with caution. To mitigate the risk of historical outliers disproportionately influencing the derivative of the polynomial (and thus the mass transfer rate estimation), the modern KWS epochs play a stabilizing role in anchoring the recent O–C trend. While a rigorously weighted analysis would be optimal, the sheer century-long baseline effectively averages out stochastic, short-term observational noise, ensuring that the macroscopic secular trends captured by both the polynomial and the Applegate-type models reflect genuine physical evolution.

4.3 Period Analysis

As mentioned previously, we divided the light curve into five segments[1]. We employed Phase Dispersion Minimization (PDM) and Generalized Lomb–Scargle (GLS) periodograms to estimate the orbital period and search for additional periodicities (Table 4.3.1). Throughout this work, we refer to the $\sim$ 36.57-day signal as the **orbital period** (P_{orb}) and to the $\sim$ 800-day signal as the **long cycle** (P_{long}).

The orbital period remains consistently close to $\sim$ 36.57 d across all segments, with Segment 2 showing the largest deviation. Although the O–C analysis (Section 4.2) reveals secular and cyclic variations, the segment-by-segment periodograms are consistent with a constant period within uncertainties. This apparent discrepancy is expected: periodograms measure an average frequency over a limited time window, while the O–C method is sensitive to cumulative phase shifts over many cycles. Given that the period change rate is small, its effect within a single segment remains below the typical PDM uncertainty ($\sim$ 0.01–0.06 d).

[1]These segments were constructed in July 2025. Since then, the KWS survey has been updated, and the newer observations are not included in the segmentation.

Segment	ΔHJD - 2400000	N	PDM $P_{\rm orb}$ (Days)	FAP (PDM)	GLS $P_{\rm long}$ (Days)	FAP (GLS)
1	17925–26743	606	36.570258 ± 0.009529	$< 10^{-3}$	547.94 ± 28.28	$< 10^{-3}$
2	37649–39671	597	36.607576 ± 0.033838	$< 10^{-3}$	295.06 ± 17.37	0.075
3	44867–55219	1278	36.569255 ± 0.017051	$< 10^{-3}$	644.42 ± 146.63	$< 10^{-3}$
4	55777–58144	1455	36.566247 ± 0.019555	$< 10^{-3}$	∼870	···
5	58315–60285	803	36.566840 ± 0.062365	$< 10^{-3}$	∼1087	$< 10^{-3}$

Table 4.3.1: Sections used to estimate the periodicities of the system. The orbital period $P_{\rm orb}$ remains consistently near ∼36.57 d. The long-cycle signal $P_{\rm long}$ varies significantly between segments and cannot be robustly constrained from this analysis alone. False alarm probabilities (FAP) are given for each period determination.

Figure 4.3.1 shows the phase-folded light curves for each segment. In contrast to the stable orbital period, the long-cycle signal cannot be consistently recovered: each segment yields a different $P_{\rm long}$ value. Segment 3 provides a formally significant detection (~ 644 d), but this value is inconsistent with the ~ 800 d signal found in the KWS data. Moreover, this segment combines heterogeneous datasets, which may introduce spurious long-period signals due to systematic offsets.

The dispersion in $P_{\rm long}$ may arise from (i) observational limitations (sampling and precision), (ii) intrinsically transient long-cycle behavior (Celedón et al. 2025), or (iii) the absence of a stable long-term periodicity in historical data. In all cases, the segmented analysis alone is insufficient to establish a coherent long cycle.

This limitation naturally motivates the use of the modern KWS dataset, which provides the most reliable constraints on long-timescale variability.

4.3.1 Long Cycle in the KWS Data

The KWS dataset is the most extensive and homogeneous photometric dataset analyzed in this work, and therefore provides the strongest constraints on long-term variability.

Applying the same methodology, we recover an orbital period fully consistent with previous estimates. In addition, a strong long-period signal near ~ 800 d is clearly detected in both the V and I_c bands (Fig. 4.3.2). The consistency across filters and methods (PDM and GLS), together with low false-alarm probabilities, confirms the robustness of this detection.

This behavior contrasts sharply with the segmented historical analysis, where

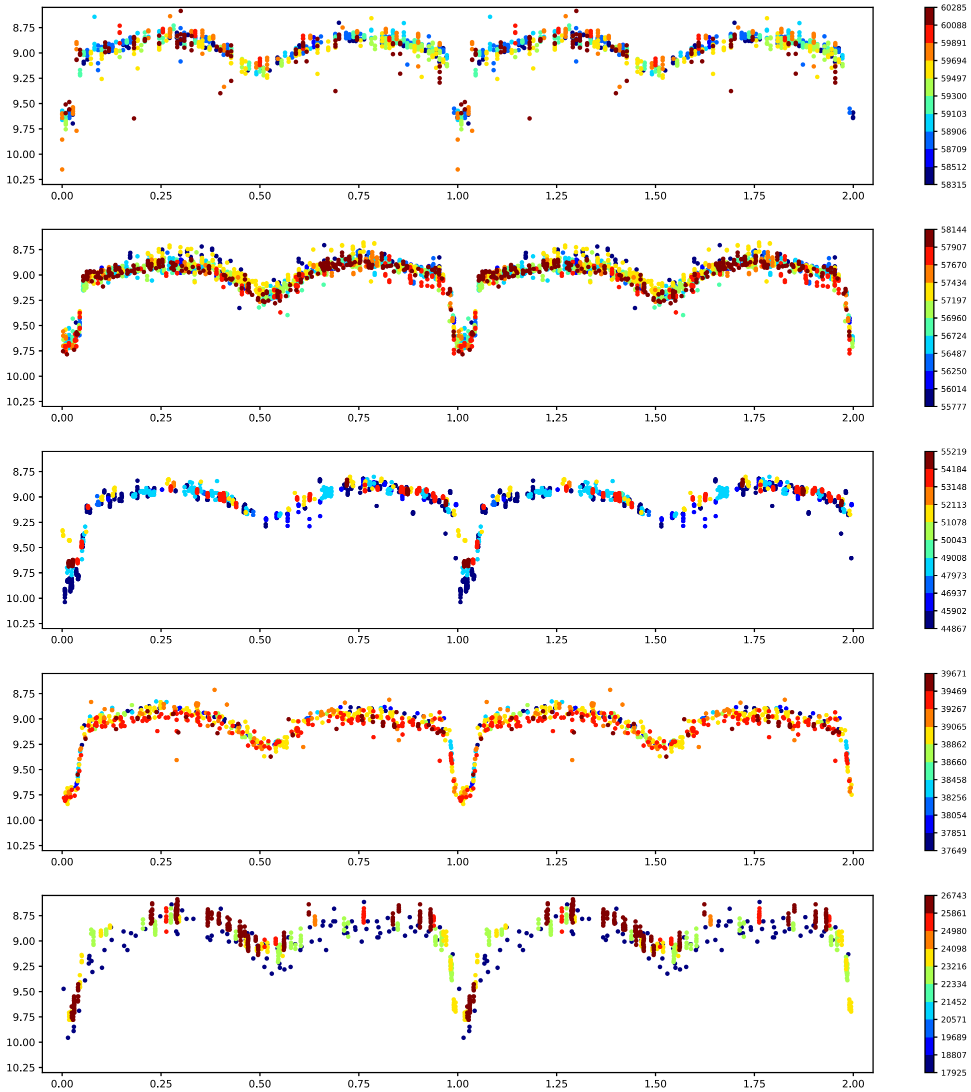

Figure 4.3.1: Light curves phase-folded using the periods listed in Table 4.3.1. The panels are ordered from the most recent (top, Segment 5, KWS V-band) to the oldest (bottom, Segment 1, visual magnitudes). The color scheme represents the epoch of each data point. Variations in the depth and shape of the primary eclipse are evident across the different epochs.

Filter	ΔHJD - 2400000	N	PDM $P_{\rm orb}$ (Days)	FAP (PDM)	GLS $P_{\rm long}$ (Days)	FAP (GLS)
V	55777–60634	2167	36.566247 ± 0.011867	$< 10^{-3}$	817.00 ± 71.92	$< 10^{-3}$
I_c	56429–60634	1342	36.568587 ± 0.016549	$< 10^{-3}$	757.10 ± 83.03	$< 10^{-3}$

Table 4.3.2: Same as Table 4.3.1, but for the KWS dataset. A consistent orbital period is detected in both filters, along with a strong long-cycle signal near ∼800 d.

$P_{\rm long}$ appears inconsistent. The improved cadence, photometric precision, and temporal coverage of the KWS data suggest that the ~ 800 d signal is likely to represent a genuine physical variability component.

To investigate the temporal evolution of this signal, we computed a weighted wavelet Z-transform (WWZ). The analysis confirms that the ~ 800 d periodicity persists over a substantial fraction of the observational baseline and increases in strength toward recent epochs (Fig. 4.3.3). The apparent weakening near the end of the dataset is likely due to data gaps, to which the WWZ method is particularly sensitive.

A thorough inspection confirmed that none of the detected peaks in the long-cycle range (300–1200 d) coincide with any of the prominent alias frequencies: the detected signal at $P_{\rm long} \approx 817$ d in the KWS V band lies between the ∼730 d alias and the one-year alias, clearly resolved from both. The independent detection at $P_{\rm long} \approx 757$ d in the I_c band further argues against an alias origin, since a common alias would be expected to appear at the same period in both bands. Both values are statistically consistent within their uncertainties (817 ± 72 and 757 ± 83 d), providing mutual corroboration that the detected signal is astrophysical.

Overall, the KWS dataset provides the strongest observational support for the presence of a long photometric cycle in SX Cas.

4.4 Light Curve Analysis

4.4.1 Full Light Curve Analysis

As described in Section 3, the light curve was divided into five segments and submitted to Professor Djurasevic[2] for detailed light-curve modeling. This analysis

[2]Professor Djurasevic determined that several data points in the datasets were spurious and discarded them.

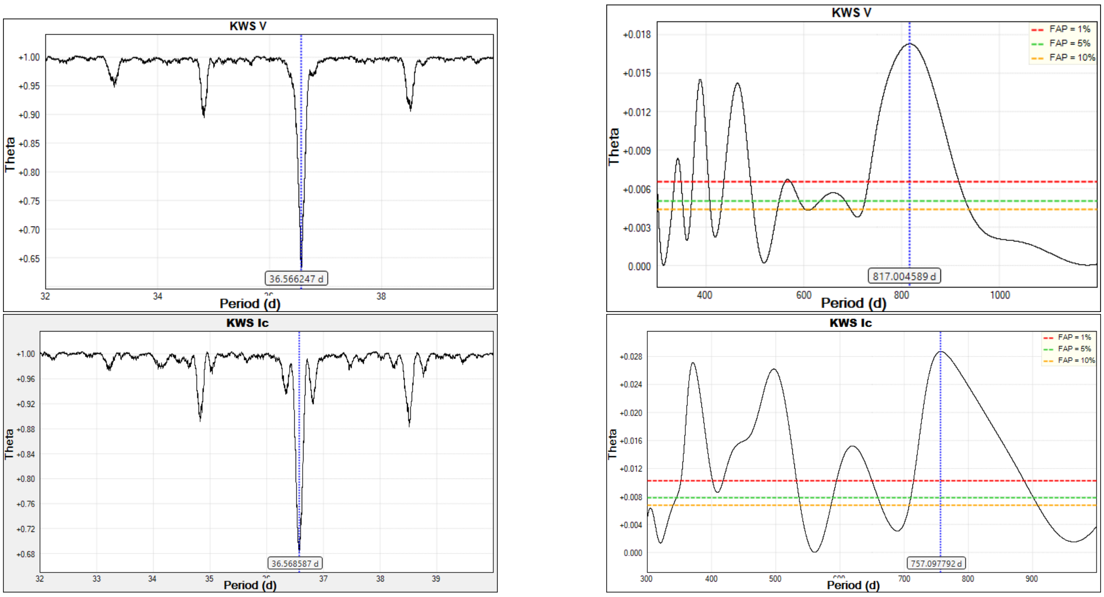

Figure 4.3.2: Periodograms for the KWS data. *Left*: PDM periodograms for V and I_c bands. *Right*: GLS periodograms showing a strong long-cycle signal near $\sim$800 d.

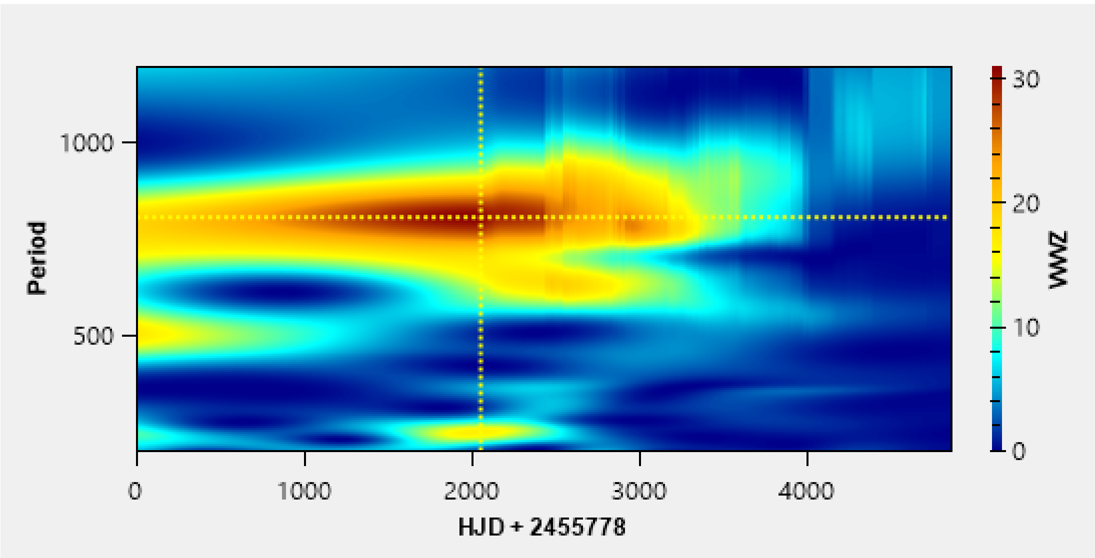

Figure 4.3.3: WWZ periodogram for KWS V data. A long-cycle signal near $\sim$800 d is detected over a significant fraction of the observational baseline.

allows us to evaluate the influence of the accretion disk on the observed variability. The results of the modeling are presented in Table 4.4.1. The contribution of each component to the light curve is shown in Fig. 4.4.1, and a visual representation of the system configuration is provided in Fig. 4.4.2. The system parameters have changed significantly over time, particularly those associated with the accretion disk. The disk morphology exhibits substantial variations across epochs, suggesting a possible connection with the unusual orbital period evolution discussed in Chapter 5.

4.4.2 Light Curve Analysis on KWS Data

As discussed above, the KWS data show evidence of the long cycle $P_{\rm long}$. A light curve analysis of these data can provide insight into the physical origin of this cycle. For this purpose, we phase-folded the KWS data with $P_{\rm long}$ as reported for the V band data in Table 4.3.2 and divided it into 10 consecutive sections, each spanning a phase window of $\Delta\phi = 0.1$ in the long cycle (i.e., Set 1 covers $\phi_{\rm long} \in [0.0, 0.1)$, Set 2 covers $[0.1, 0.2)$, and so on through Set 10 covering $[0.9, 1.0)$). Each section therefore represents one tenth of the full long cycle, and the orbital light curve within each section is constructed from all KWS observations falling within that phase window. These 10 orbital light curves were submitted to Professor Djurasevic for light-curve modeling, allowing us to track how the system's structural parameters evolve as a function of the long-cycle phase. The results are shown visually in Figs. 4.4.3 and 4.4.4. The analysis indicates that the system is undergoing significant structural changes in its accretion disk across $P_{\rm long}$, suggesting a physical connection between the long cycle and the evolving disk morphology.

4.4.3 Comparison Between Historical and KWS-Based Models

In order to assess the consistency and temporal evolution of the system parameters, we compare the classical solution of Andersen et al. (1988) with the results obtained from the two independent light-curve modeling approaches performed by Djurašević: (i) the historical multi-epoch analysis (Table 4.4.1), and (ii) the phase-resolved modeling based on the KWS dataset (Table 4.4.2).

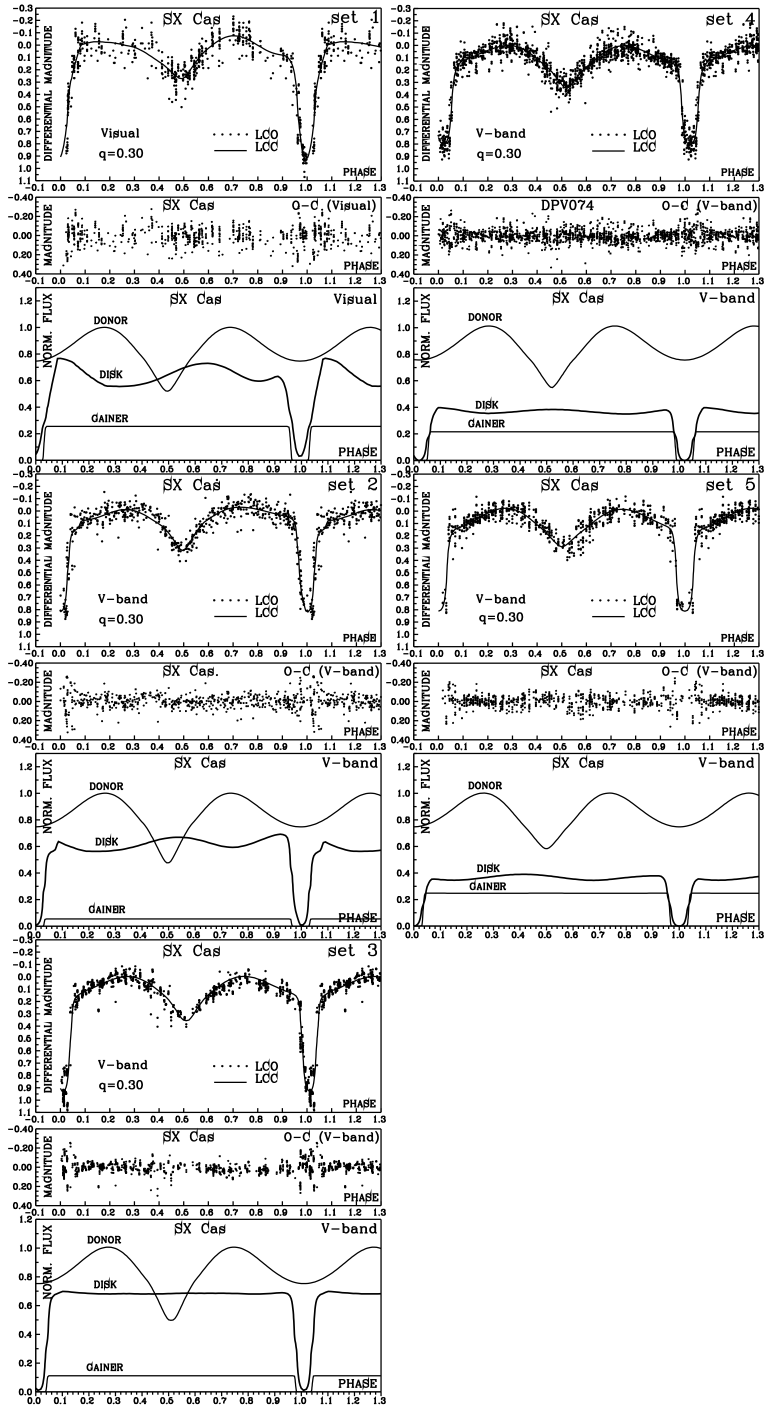

Figure 4.4.1: Fits to the 5 segments of the light curve with the corresponding contributions from the disk, donor, and gainer.

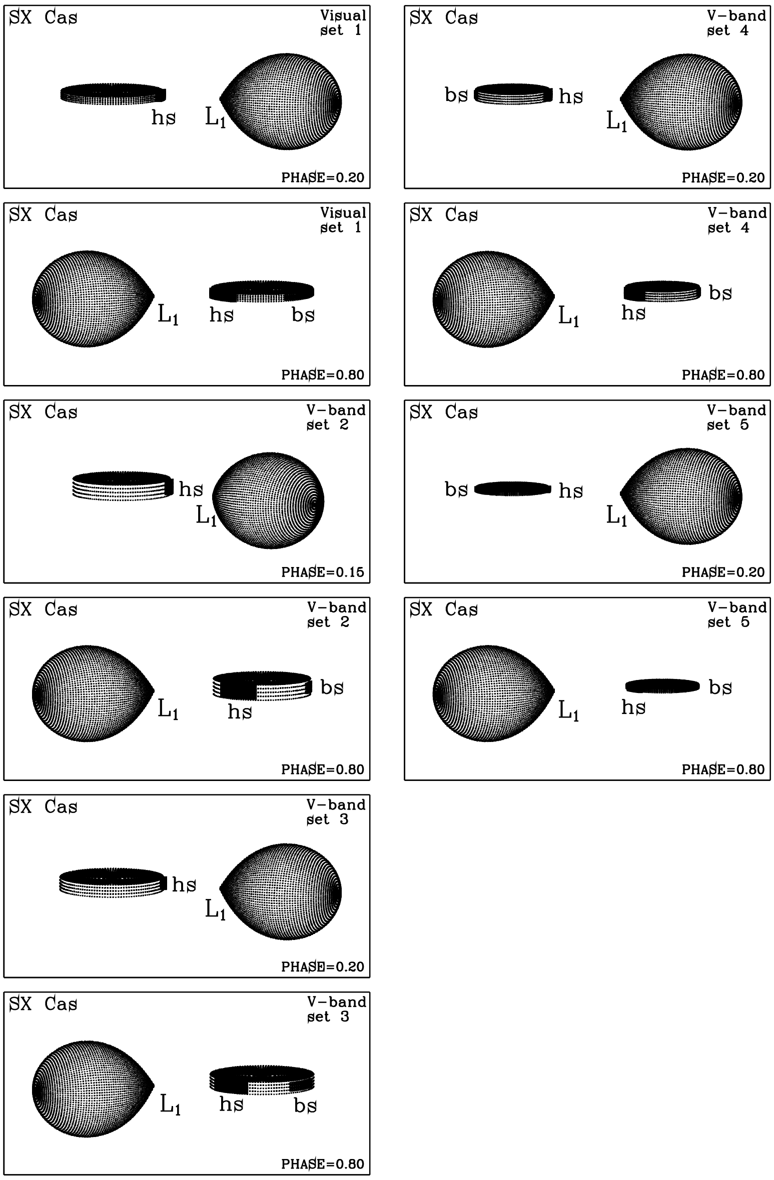

Figure 4.4.2: Visual representation of the system configuration corresponding to the results listed in Table 4.4.1. Each panel shows the configuration at two representative orbital phases (near 0.20 and 0.60) for each temporal segment; the exact phase displayed may differ slightly from 0.20 when data coverage did not permit a solution at precisely that value (e.g., Set 2 is shown at phase 0.15). Labels: hs = hot spot, bs = bright spot, L_1 = inner Lagrangian point.